Smith-Magenis syndrome protein Rai1 regulates body weight homeostasis through hypothalamic Bdnf-producing neurons and TrkB signalling

Sehrish Javed[1,2], Ya-Ting Chang[1,2], Yoobin Cho[1,2], Yu-Ju Lee[1,2], Hao-Cheng Chang[1,2], Minza Haque[1,2], Yu Cheng Lin[1,2], Wei-Hsiang Huang[1,2,*]

Affiliations:

[1]Department of Neurology and Neurosurgery, Centre for Research in Neuroscience, McGill University, Montréal, QC H3G 1A3, Canada

[2]Brain Repair and Integrative Neuroscience Program, The Research Institute of the McGill University Health Centre, Montréal, QC H3G 1A3, Canada

*Corresponding author. Email: wei-hsiang.huang@mcgill.ca

Abstract

Retinoic acid-induced 1 (*RAI1*) haploinsufficiency causes Smith-Magenis syndrome (SMS), a genetic disorder with symptoms including hyperphagia, hyperlipidemia, severe obesity, and autism phenotypes. Rai1 is a transcriptional regulator with a pan-neural expression pattern and hundreds of downstream targets. The mechanisms linking neural *Rai1* to body weight regulation remain unclear. Here we find that hypothalamic brain-derived neurotrophic factor (Bdnf)-TrkB signalling is disrupted in SMS ($Rai1^{+/-}$) mice. Selective Rai1 loss from all Bdnf-producing cells or from Bdnf-producing neurons in the paraventricular nucleus of the hypothalamus (PVH) induced obesity in mice. Electrophysiological recordings revealed that *Rai1* ablation increased inhibitory synaptic transmission to PVH^{Bdnf} neurons and decreased intrinsic neuronal excitability. Chronic treatment of SMS mice with a partial agonist of tropomyosin receptor kinase B (TrkB), the cognate Bdnf receptor, delayed obesity onset. This treatment also partially rescued disrupted lipid profiles, insulin intolerance, and stereotypical repetitive behaviour in SMS mice. These data argue that Rai1 regulates body weight and metabolic function through hypothalamic Bdnf-producing neurons and that targeting TrkB signalling might improve associated SMS phenotypes.

Introduction

Obesity is an increasing global concern: 20% of the world's adult population is expected to become obese by 2025 if current trends persist (Collaboration, 2017). However, the complex environmental, behavioural, and genetic contributions to obesity make this a difficult condition to model and address. Monogenic obesity disorders provide a consistent system where the pathophysiology, genetic predisposition, and neurobiology underlying phenotypes can potentially provide insights that translate to polygenic obesity (Loos & Yeo, 2022).

One such monogenic disorder is Smith-Magenis syndrome (SMS; OMIM #182290) (Smith *et al*, 1986), a neurogenetic condition frequently associated with obesity. 80% of SMS cases are caused by interstitial deletions of the 17p11.2 chromosomal region containing a dosage-sensitive gene, *retinoic acid-induced 1* (*RAI1*) (Slager *et al*, 2003). More than 90% of SMS patients are overweight (40% > 95th percentile weight, 40% > 85th percentile weight) and exhibit over-eating tendencies by adolescence (Alaimo *et al*, 2015; Burns *et al*, 2010; Gandhi *et al*, 2022). 20% of SMS patients do not have 17p11.2 deletions but instead carry *RAI1* point mutations that are still frequently associated with obesity (Boot *et al*, 2021; Edelman *et al*, 2007). These clinical data indicate that RAI is critical for energy homeostasis underlying body weight regulation.

The human RAI1 protein shares >80% sequence identity with the mouse Rai1 protein, allowing us to study Rai1 function *in vivo* (Huang *et al*, 2016; Javed *et al*, 2020). We previously found that *Rai1* encodes a transcriptional regulator that binds to the promoter or enhancer regions of its target genes, most of which are involved in neurodevelopment and synaptic transmission (Huang *et al.*, 2016). SMS (*Rai1*$^{+/-}$) mice exhibit obesity associated with hyperphagia and increased adiposity (Burns *et al.*, 2010; Huang *et al.*, 2016). Interestingly, Rai1 may have a sexually

61 dimorphic function, as female SMS mice exhibit more pronounced obesity than males (Burns *et*
62 *al.*, 2010; Huang *et al.*, 2016).

63 Using a homozygous *Rai1* conditional knockout (*Rai1*-cKO) mice, we found that *Rai1* deletion
64 in either subcortical excitatory neurons (vGlut2$^+$) or single-minded homolog 1 (Sim1$^+$) neurons
65 induced obesity in mice (Huang *et al.*, 2016). Sim1$^+$ neurons reside in several brain regions
66 including the nucleus of the lateral olfactory tract, the supraoptic nucleus, the medial amygdala,
67 and the paraventricular nucleus of the hypothalamus (PVH), a region that is critical for body
68 weight regulation (Balthasar *et al*, 2005). Sim1$^+$ neurons in the PVH are composed of several
69 molecularly defined cell types including those that express oxytocin, vasopressin, corticotropin-
70 releasing hormone, somatostatin, melanocortin-4-receptor (MC4R), growth hormone-releasing
71 hormone (GHRH), or brain-derived neurotrophic factor (Bdnf) (An *et al*, 2015). Deleting *Bdnf*
72 from the PVH results in hyperphagic obesity and reduced locomotion (An *et al.*, 2015). While
73 PVH neuronal activity is reduced during feeding (Xu *et al*, 2019), activation of PVH^{Bdnf} neurons
74 results in weight loss (Wu & Xu, 2022). We recently found that Rai1 promotes *Bdnf* expression
75 in hypothalamus throughout life (Javed *et al*, 2021). We hypothesized that Rai1 may be
76 connected to Bdnf-producing neurons in PVH, explaining how a neural transcription factor
77 regulates body weight homeostasis.

78 Bdnf regulates energy metabolism by binding to its cognate receptor tropomyosin receptor
79 kinase B (TrkB) (An *et al.*, 2015) and may thus provide a potential therapeutic target for SMS.
80 However, the link between *Rai1,* Bdnf, and SMS symptoms is currently unclear. Patients
81 carrying monogenic mutations in either *BDNF* (Gray *et al*, 2006) or *NTRK2* (encoding TrkB)
82 (Yeo *et al*, 2004) experience severe hyperphagic obesity. Moreover, obesity and associated
83 metabolic dysfunction such as impaired glucose and insulin sensitivity are correlated with

84 impaired PI3K-Akt pathway, a TrkB downstream target (Su *et al*, 2021). Given that (1) *Bdnf*
85 overexpression during early embryonic development or (2) targeting *Bdnf* overexpression to the
86 PVH of adolescent SMS (*Rai1*$^{+/-}$) mice protected them from weight gain and metabolic defects
87 (Javed *et al.*, 2021), and that (3) a point mutation in *RAI1* disrupts its ability to transcriptionally
88 enhance *Bdnf* expression *in vitro* (Abad *et al*, 2018), pharmacological targeting of Bdnf signaling
89 is an attractive and yet unexplored therapeutic avenue for SMS.

90 Building on our previous discoveries, here we examine the neurobiological functions of Rai1 in
91 Bdnf-producing neurons, specifically those that reside in the PVH. Importantly, we evaluated the
92 involvement of the Bdnf-TrkB pathways in SMS pathogenesis using a small molecule drug
93 (LM22A-4) to enhance TrkB signalling. Our work indicates that PVH^{Bdnf} neurons depend on
94 Rai1 to maintain normal neuronal activity and regulate body weight homeostasis, and TrkB
95 signalling dysfunction contributes to obesity associated with SMS mice.

96

97 **Results**

98 ***Rai1* deficiency dysregulates specific downstream targets of neurotrophin in the mouse**
99 **hypothalamus**

100 Multiple lines of evidence indicated that SMS mice show decreased *Bdnf* mRNA expression in
101 the hypothalamus (Burns *et al.*, 2010; Huang *et al.*, 2016; Javed *et al.*, 2021). To determine if
102 Bdnf protein levels were consequently altered in the hypothalamus, we performed enzyme-linked
103 immunosorbent assay (ELISA) and found that Bdnf protein levels were significantly reduced in
104 7-week-old pre-symptomatic SMS mice relative to controls (**Fig 1A**). To quantify if molecular
105 pathways associated with Bdnf-TrkB signalling were altered, we subjected hypothalamic tissue
106 lysates from 7-week-old pre-obese SMS and control (Ctrl) mice to reverse phase protein array
107 (RPPA) (**Fig 1B**). We found that control and SMS samples clustered separately in principle
108 component analysis (**Fig 1C**).

109 Hierarchical clustering analysis indicated that the majority of differentially expressed
110 phosphorylated proteins (**Fig 1D**) and total proteins (**Figure 1—figure supplement 1**) were
111 downregulated in SMS mice. We mapped all proteins, as well as phospho-proteins, that were
112 differentially expressed in Ctrl and SMS samples onto the interconnected biological network and
113 identified a subset of connected nodes downregulated in SMS (FDR < 10e-5) belong to the
114 neurotrophin, PI3K-Akt, and mTOR signalling pathways (**Fig 1E**). These pathways are known to
115 play a critical role in regulating body weight homeostasis and can be activated by Bdnf either
116 directly (neurotrophin pathway) or indirectly (PI3K-Akt and mTOR pathways) (Cota *et al*, 2006;
117 Schultze *et al*, 2012). The expression levels of PIK3CA, a common node in these pathways, were
118 significantly reduced in the SMS mice compared to controls (**Fig 1F**). Moreover, the expression
119 levels of phosphorylated NF-κB (nuclear factor-kappa B), a downstream target of the

120 neurotrophin pathway, were significantly reduced in the SMS group (**Fig 1G**). Together, these
121 results suggest that *Rai1* loss impairs specific pathways, including neurotrophin signalling, and
122 indicate that dysfunction of Bdnf-producing cells could contribute to SMS pathogenesis.

123

124 **Bdnf-producing cells depend on Rai1 to regulate body weight homeostasis**

125 To target Bdnf-producing cells, we used a *Bdnf*$^{Cre/+}$ mouse line that carries a viral 2A
126 oligopeptide and Cre recombinase immediately upstream of Bdnf's endogenous STOP codon
127 (Tan *et al*, 2016). We crossed the *Bdnf*$^{Cre/+}$ mice with tdTomato-Ai9 reporter mice and found that
128 Ai9 signals faithfully reflected endogenous Bdnf protein expression in the PVH (**Figure 2—**
129 **figure supplement 1A-E**). More than 50% of Bdnf-producing cells within the PVH were
130 positive for phosphorylated TrkB (p-TrkB) (**Figure 2—figure supplement 1F**). Moreover, 20%
131 of p-TrkB^{+} PVH cells express Bdnf, suggesting that Bdnf could have an autocrine mode of action
132 in this cell type (**Figure 2—figure supplement 1F-J**). We also found that Rai1 is expressed in
133 PVH^{Bdnf} cells that are distinct from larger magnocellular cells such as the PVH oxytocin neurons
134 (**Figure 2—figure supplement 2A-I**). Specifically, 55% of PVH^{Bdnf} neurons express Rai1,
135 whereas only 2% of PVH^{Oxytocin} neurons express Rai1 (**Figure 2—figure supplement 2I**). These
136 data suggest that Rai1 is enriched in Bdnf-producing neurons in the mouse PVH.

137 To determine if Bdnf-producing cells depend on Rai1 to regulate body weight, we deleted one or
138 both copies of *Rai1* using the *Bdnf*$^{Cre/+}$ and the conditional *Rai1*$^{fl/fl}$ mice (Huang *et al.*, 2016) (**Fig**
139 **2A, Figure 2—figure supplement 3A**). Conditional knockout mice (cKO: *Bdnf*$^{Cre/+}$*; Rai1*$^{fl/fl}$)
140 showed a significant reduction in Rai1 expression in PVH^{Bdnf} neurons compared to controls (**Fig**
141 **2B-C**, **Figure 2—figure supplement 3B)**. The total number of Bdnf-producing cells in the PVH

142 remained similar in Ctrl and cKO mice (**Figure 2—figure supplement 3C**), indicating that Rai1
143 loss did not affect PVH neurogenesis or survival.

144 We monitored body weight weekly and found that male and female cKO mice showed a
145 significant increase in body weight beginning at 15 weeks of age when compared to controls
146 (Ctrl: *Bdnf*$^{Cre/+}$) (**Fig 2D**, **Figure 2—figure supplement 4A**). However, conditional *Rai1*
147 heterozygous mice (*Bdnf*$^{Cre/+}$*; Rai1*$^{fl/+}$) did not show a pathological increase in body weight
148 (**Figure 2—figure supplement 3D**, **Figure 2—figure supplement 4B**), suggesting that non-
149 Bdnf-producing cells also contribute to SMS pathogenesis. EcoMRI found that 26-week-old
150 cKO male and female mice showed an increased proportion of fat mass but not lean mass (**Fig**
151 **2E**, **Figure 2—figure supplement 4C**). Further dissection of fat tissues from different organs
152 showed an increased mass of subcutaneous inguinal (S.C. Ing.) fat in cKO mice of both sexes
153 and increased mass of epididymal adipose tissues (eWAT) in female cKOs (**Fig 2F**, **Figure 2—**
154 **figure supplement 4D**).

155 In contrast, the total mass of brown adipose tissue (BAT) remained unchanged between groups
156 (**Fig 2F**, **Figure 2—figure supplement 4D**). In both male and female cKO mice, we found
157 hypertrophic eWAT adipocytes (**Fig 2G**, **Figure 2—figure supplement 4E**) and elevated blood
158 leptin levels (**Fig 2H**, **Figure 2—figure supplement 4F**). However, there was no significant
159 alteration in blood lipids such as triglycerides (TG), high-density lipoprotein (HDL), low-density
160 lipoproteins (LDL), and very low-density lipoprotein (VLDL) in either male or female cKO mice
161 (**Figure 2—figure supplement 3E-G**, **Figure 2—figure supplement 4G-I)**. Altogether, these
162 data suggest that obesity caused by ablating *Rai1* from Bdnf-producing cells is associated with
163 increased fat mass, fat deposition, and leptin levels.

164 Obesity could result from increased food intake, reduced energy expenditure, or both. Similar to
165 SMS mice, male and female cKO mice did not have defects in respiratory exchange rates when
166 measured by indirect calorimetry (**Figure 2—figure supplement 3H**, **Figure 2—figure**
167 **supplement 4J**). Interestingly, cKO mice showed sex-specific differences in energy expenditure.
168 During the dark phase, female cKO mice showed a reduction in energy expenditure (**Fig 2I**) and
169 decrease in total locomotor activity (**Fig 2J**). In contrast, total food intake remained unchanged
170 (**Fig 2K**). Male cKO mice became hyperphagic (**Figure 2—figure supplement 4K**), showed
171 increased energy expenditure during the dark phase (**Figure 2—figure supplement 4L**), and
172 exhibited normal locomotor activity when compared to controls (**Figure 2—figure supplement**
173 **4M**). These results suggest that obesity in male cKO mice is attributable to overeating despite an
174 increase in energy expenditure.

175 To determine if Rai1 loss from Bdnf-producing cells impacts metabolic function, a glucose
176 tolerance test (GTT) was performed. Interestingly, cKO mice of both sexes showed normal blood
177 glucose levels right before the test but became hyperglycemic 20 minutes (female cKO) and 45
178 minutes (male cKO) after glucose administration (**Fig 2L**, **Figure 2—figure supplement 4N**).
179 This change was accompanied by a significantly higher area under the curve (AUC) for both
180 groups (**Figure 2—figure supplement 3I**, **Figure 2—figure supplement 4O**). While the male
181 cKO mice remained hyperglycemic throughout the GTT (**Figure 2—figure supplement 4P**), the
182 glucose levels in female cKO mice returned to normal towards the end (**Fig 2L**). We also found
183 increased blood insulin levels during the GTT in both sexes (**Figure 2—figure supplement 3J**,
184 **Figure 2—figure supplement 4P**). In the insulin tolerance test (ITT), female cKO mice showed
185 moderately elevated glucose levels 20 minutes into the test (**Figure 2—figure supplement 3K**).
186 By contrast, male cKO mice showed considerably higher glucose levels than controls in the ITT

187 (~6.5 ng/ml for cKO and ~2.0ng/ml for Ctrl) during the 60- to 120-minute intervals (**Figure 2—**
188 **figure supplement 4Q**). Altogether, these experiments demonstrate that Bdnf-producing cells
189 depend on Rai1 to regulate body weight, adiposity, glucose and insulin tolerance in mice.

190

191 ***Rai1* deletion reduces PVH^{Bdnf} neuronal excitability**

192 Bdnf-producing neurons are widely distributed in the hypothalamus, being found in the
193 dorsomedial hypothalamus (Unger *et al*, 2007), ventromedial hypothalamus (Xu *et al*, 2003), and
194 PVH (An *et al.*, 2015). To understand how *Rai1* loss affects intrinsic neuronal excitability and
195 synaptic transmission of PVH^{Bdnf} neurons that underlie energy homeostasis (An *et al.*, 2015), we
196 fluorescently labelled them with Cre-dependent tdTomato (**Fig. 3A**). We found that a
197 hyperpolarized step followed by increasing the holding voltage at resting membrane potentials
198 (Rm) was able to initiate rebound firing or rebound repetitive firing in most PVH^{Bdnf} neurons
199 (**Figure 3—figure supplement 1A**). Hyperpolarization-induced I_H currents and low
200 depolarization events were observed in some PVH^{Bdnf} neurons (**Figure 3—figure supplement**
201 **1A**). cKO PVH^{Bdnf} neurons showed reduced action potential (AP) firing frequency at a holding
202 voltage of -60mV compared to Ctrl PVH^{Bdnf} neurons (**Fig 3B-C**). The resting membrane
203 potential (Rm) of cKO (-52mV) neurons showed a 10mV positive shift compared to Ctrl neurons
204 (-62mV) (**Fig 3D**). We also found that fewer cKO PVH^{Bdnf} neurons showed spontaneous firing at
205 Rm (**Fig 3E**, Ctrl:10/13; cKO:5/12) and at holding voltage of -70mV (**Fig 3F**, Ctrl:6/12;
206 cKO:1/12) compared to Ctrl PVH^{Bdnf} neurons. The threshold of the first AP initiated by a ramp
207 current injection (1 nA/sec) from Rm was significantly increased in cKO neurons (**Fig 3G-H**).
208 Because the higher the holding voltage is, the narrower the shoulder and the lower the amplitude
209 of APs are (**Figure 3—figure supplement 1B**), we compared the AP waveforms at a holding

210 voltage of -60mV, close to the Rm of both genotypes. The AP of the cKO group exhibited a
211 lower peak amplitude (measuring from the threshold to peak) (**Fig 3I**), a normal threshold (**Fig**
212 **3J**), and half-width (**Figure 3—figure supplement 1C**). We found that both passive and AP
213 properties of cKO PVH^{Bdnf} neurons were altered. The Rm of cKO neurons shifted to a more
214 positive voltage than the gating threshold of voltage-gated sodium channels (6/12 were more
215 positive than -55mV), which was unfavourable for their transition from the inactivation state to
216 the closed state. Combined with the higher AP threshold of cKO neurons, these changes
217 contribute to a decreased excitability in cKO PVH^{Bdnf} neurons.

218 PVN neurons receive glutamatergic and GABAergic inputs and are tonically inhibited by
219 GABAergic neurons (Colmers & Bains, 2018; Gao *et al*, 2017). The rightward shift of the
220 probability of miniature inhibitory postsynaptic current (mIPSC) frequency indicated that cKO
221 PVH^{Bdnf} neurons received a higher frequency of inhibitory inputs, although the average
222 frequency (**Fig 3K**) was not significantly different between groups. The probability of mIPSC
223 amplitude also showed a right shift, suggesting an increased mIPSC postsynaptic response (**Fig**
224 **3L, Figure 3—figure supplement 1D**). Furthermore, we observe an increased area under the
225 curve (**Fig 3M**), indicating that *Rai1* loss induced a larger total outward current upon the
226 inhibitory inputs. Interestingly, we found that cKO PVH^{Bdnf} neurons had a smaller cellular
227 diameter (**Figure 3—figure supplement 1E**), indicating that the increased inhibitory currents
228 were unlikely due to changes in passive membrane properties associated with increased cell size.
229 Overall, our data argue that *Rai1* deletion decreases the excitability of PVH^{Bdnf} neurons and
230 likely increases pre-synaptic inhibitory transmission and post-synaptic inhibitory responses,
231 resulting in decreased AP firing.

232

233 **Rai1 expression is necessary for PVH^{Bdnf} neurons to regulate energy homeostasis**

234 Reduced PVH^{Bdnf} neuronal activity in cKO mice suggested that Rai1 loss in Bdnf-producing
235 PVH neurons might be sufficient to induce defective energy homeostasis *in vivo*. To test this
236 hypothesis by deleting Rai1 only in PVH^{Bdnf} neurons but not other Bdnf-producing cells, we
237 performed PVH^{Bdnf}-specific *Rai1* deletion using a CRISPR/Cas9 system packaged into AAV9.
238 Two viruses were delivered; one encoding a reporter molecule (GFP) and three single guide
239 RNAs targeting the *Rai1* gene (sgRai1), and the other carrying Cre-dependent *Staphylococcus*
240 *aureus* CRISPR-associated protein 9 (saCas9) (**Fig 4A**). Hereafter, our experiments focus on
241 female SMS mice since they showed more consistent defects in fat distribution (Burns *et al.*,
242 2010) and body weight regulation (Huang *et al.*, 2016) than males. Bilateral administration of
243 two AAVs into the PVH of female *Bdnf*$^{Cre/+}$ mice (Exp group) resulted in a significant loss of
244 Rai1 protein expression in PVH^{Bdnf} neurons when compared to *Bdnf*$^{Cre/+}$ mice injected with an
245 AAV encoding the sgRai1 and GFP (Ctrl group) (**Fig 4B-C**, **Figure 4—figure supplement 1A**).
246 Quantification of AAV-infected (GFP^{+}) Bdnf neurons showed that while the total number of
247 Bdnf^{+} (**Figure 4—figure supplement 1B**) and Bdnf^{+} GFP^{+} (**Figure 4—figure supplement 1C**)
248 cells was not different in the two groups, the percentage of AAV-infected Bdnf^{+} cells that
249 express Rai1 was significantly reduced in the Exp group (**Fig 4C**, **Figure 4—figure supplement**
250 **1D-E**). Deleting *Rai1* from the PVH^{Bdnf} neurons resulted in a significant increase in body weight
251 beginning at 17 weeks of age (**Fig 4D**). Similar to the cKO (*Bdnf*$^{Cre/+}$*; Rai1*$^{fl/fl}$) mice, obesity in
252 26-week-old Exp mice was due to increased fat mass (**Fig 4E**) and more specifically, increased
253 subcutaneous inguinal (S.C. ing) and epididymal white adipose tissues (eWAT) but not BAT
254 (**Fig 4F**). We also found that eWAT adipocytes became hypertrophic (**Fig 4G**). Similar to the
255 cKO mice, food intake did not differ between Exp and Ctrl groups (**Fig 4H**), likely due to the

256 high level of satiety signals in the brain caused by increased blood leptin levels (**Fig 4I**). We also
257 found that energy expenditure (**Fig 4J**), respiratory exchange rate (**Figure 4—figure**
258 **supplement 1F**), and blood lipid parameters, including TG (**Figure 4—figure supplement 1G**),
259 HDL (**Figure 4—figure supplement 1H**), LDL and VLDL levels (**Figure 4—figure**
260 **supplement 1I**), were similar in Exp and Ctrl groups, consistent with the cKO data (**Figure 4—**
261 **figure supplement 14**). Interestingly, Exp mice showed significantly less locomotor activity
262 during the dark phase than the Ctrl mice (**Fig 4K**). A GTT indicated that Exp mice have a
263 hyperglycemic profile (**Fig 4L**), accompanied by a slightly higher area under the curve for blood
264 glucose levels (p=0.05) (**Fig 4M**). Insulin levels in Exp mice were also significantly elevated 15
265 minutes after glucose administration (**Fig 4N**).

266 While Exp mice showed a trend towards increased glucose levels in insulin tolerance tests, the
267 change was not statistically different (**Figure 4—figure supplement 1J**). Altogether, these
268 experiments indicate that conditional deletion of Rai1 from PVH^{Bdnf} neurons during adolescence
269 impairs the regulation of body weight, adiposity, glucose tolerance, and locomotion. These
270 changes recapitulate most phenotypes observed in cKO mice with *Rai1* deleted in Bdnf-
271 producing cells from early development.

272

273 **Pharmacologically enhancing TrkB signalling partially alleviates obesity in SMS mice**

274 Our findings so far indicate that multiple pathways, including neurotrophin signalling, are
275 dysregulated in SMS mice, and that Rai1 loss from Bdnf-producing cells, including PVH^{Bdnf}
276 neurons, impairs energy homeostasis *in vivo*. Next we sought to examine the contribution of
277 Bdnf-TrkB dysfunction in SMS pathogenesis by pharmacologically activating downstream
278 targets of the Bdnf-TrkB pathway.

279 We systematically treated mice with LM22A-4, a small molecule Bdnf loop domain mimetic
280 (Massa *et al*, 2010). To measure the bioavailability of LM22A-4 in the SMS brain, we
281 simultaneously administered LM22A-4 intranasally (5 mg/kg body weight) and intraperitoneally
282 (50 mg/kg body weight), using the highest doses used in previous studies (Canals *et al*, 2004;
283 Chang *et al*, 2006; Gu *et al*, 2022; Kron *et al*, 2012; Ogier *et al*, 2007). We then harvested
284 forebrain and hypothalamic tissues one- or three-hours after drug administration. Spectrometric
285 analysis found a significantly higher LM22A-4 concentration in both brain regions one-hour
286 post-treatment, while its concentration decreased three hours after treatment (**Figure 5—figure**
287 **supplement 1A**). Consistent with the reduced neurotrophin signalling observed in our proteomic
288 analysis, saline-treated SMS mice showed reduced phosphorylated-Akt (p-Akt; **Fig 4A**, **Figure**
289 **5—figure supplement 1B**) levels in the hypothalamus. LM22A-4 treatment significantly
290 increased the levels of p-Akt in the SMS mice 1-hr post-treatment (**Fig 4A**, **Figure 5—figure**
291 **supplement 1B**), indicating increased signalling downstream of the Bdnf-TrkB pathway.

292 We next examined if chronic LM22A-4 treatment was sufficient to reverse or modify the
293 progression of the obesity phenotype in adult SMS mice. Specifically, we treated SMS mice
294 daily from 8 to 14 weeks of age, during which SMS mice began to gain significantly more
295 weight. Saline-treated SMS mice (**Fig 5C**) were significantly heavier than saline-treated control
296 mice from 9 weeks of age onward. Interestingly, LM22A-4-treated SMS mice showed a similar
297 body weight to saline-treated control littermates until 13 weeks of age but became obese by 14
298 weeks of age (**Fig 5D**). Consistent with a partial rescue, LM22A-4-treated SMS mice were
299 significantly less obese than saline-treated SMS mice throughout the treatment period (**Fig 5E**).
300 Control mice treated with LM22A-4 did not show a further reduction in body weight (**Figure**

301 **5—figure supplement 1C**), indicating that the therapeutic effects were specific to SMS
302 pathogenesis.

303 We measured food intake and found that LM22A-4 did not significantly rescue increased food
304 intake in SMS mice. (**Fig 5F**). SMS mice showed normal energy expenditure (**Figure 5—figure**
305 **supplement 1D**) and respiratory exchange rate (**Figure 5—figure supplement 1E**), neither of
306 which was altered by LM22A-4 treatment. Interestingly, we did observe a partial rescue of
307 locomotor activity in LM22A-4-treated SMS mice that was not significantly different from
308 saline-treated Ctrl or SMS mice (**Fig 5G**). We also found that LM22A-4 treatment partially
309 rescued fat deposition (**Fig 5H**) and completely rescued HDL levels (**Fig 5I**) in SMS mice.
310 During an insulin tolerance test, we found that saline-treated SMS mice showed increased
311 baseline insulin levels (**Fig 5J**) and blood glucose levels during the test (**Fig 5K**), both of which
312 were partially rescued by LM22A-4 treatment.

313 In addition to a deficit in energy homeostasis, SMS mice showed two highly reproducible
314 behavioral deficits: increased stereotypic rearing in the open field and decreased social
315 dominance in the tube test (Huang *et al*, 2018; Rao *et al*, 2017). Saline-treated SMS mice
316 showed significantly more rearing behavior when compared to the saline-treated controls (**Fig**
317 **5L**). Interestingly, LM22A-4 treatment reduced the repetitive rearing behaviour in SMS mice
318 **(Fig 5L**). LM22A-4 treatment did not change repetitive behaviors in control mice (**Figure 5—**
319 **figure supplement 1F**), suggesting the effect is specific to *Rai1* haploinsufficiency. However,
320 we did not observe a rescue of social dominance deficits in SMS mice (**Figure 5—figure**
321 **supplement 2A-E**). Together, these data indicate that LM22A-4 treatment delayed the onset of
322 obesity and fully rescued repetitive behaviour in SMS mice, suggesting that Bdnf-TrkB

323 signalling dysfunction contributes to changes in the mouse SMS brain linked to obesity and
324 behavioral phenotypes.

325

326 **Discussion**

327 The hypothalamus, and Bdnf-TrkB signalling in this region, control body weight by regulating
328 the intricate balance between energy intake and expenditure (Xu & Xie, 2016). The role of Bdnf-
329 producing neurons in human obesity disorders and how the activity of these cells is regulated
330 remained poorly studied. We found that Rai1 deficiency, linked to Smith-Magenis syndrome
331 (SMS), regulates Bdnf expression and maintains intrinsic excitability and inhibitory synaptic
332 transmissions in PVH^{Bdnf} neurons.

333 Consistent with this mechanism, we found that removing Rai1 from Bdnf-producing neurons or
334 PVH^{Bdnf} neurons results in imbalanced energy homeostasis and results in obesity. A small
335 molecule drug LM22A-4 led to increased Akt phosphorylation and partially rescued locomotor
336 activity, insulin intolerance, and HDL levels, while delaying the onset of obesity in SMS mice.
337 These findings highlight a potential role for hypothalamic Bdnf-producing neurons, specifically
338 PVH^{Bdnf} neurons, in SMS pathogenesis and highlight Bdnf signalling as a potentially druggable
339 pathway to improve energy homeostasis defects and repetitive behaviours commonly observed in
340 SMS patients (Burns *et al.*, 2010; Moss *et al*, 2009).

341 The involvement of different PVH subtypes in human obesity is only beginning to be elucidated.
342 Dysfunction of oxytocin PVH neurons is linked to the Prader-Willi syndrome (Lee *et al*, 2012),
343 another genetic disorder associated with obesity. Since Rai1 expression is enriched in PVH^{Bdnf}

344 neurons but not PVH^{Oxytocin} neurons, our data suggest that distinct pathophysiological
345 mechanisms underlie SMS and Prader-Willi syndrome.

346 Conditional knockout analysis allowed us to specifically map the cell-specific origin of
347 neuropathological phenotypes, such as SMS-like symptoms in mice. Our previous work found
348 that deleting *Rai1* from cortical excitatory neurons using an *Emx1*^{Cre} allele (Gorski *et al*, 2002),
349 from the GABAergic neurons using a *Gad2*^{Cre} allele (Taniguchi *et al*, 2011), or from astrocytes
350 using a *GFAP*^{Cre} allele (Garcia *et al*, 2004) did not induce SMS-like obesity (Huang *et al.*, 2016).
351 In contrast, obesity could be induced by ablating *Rai1* from Sim1-lineage neurons and, to a lesser
352 extent, SF1-lineage neurons (Huang *et al.*, 2016). This analysis suggests that Rai1 expression in
353 PVH is more important than in ventromedial nucleus of the hypothalamus (VMH) for body
354 weight regulation. Interestingly, embryonic deletion of *Bdnf* from SF1-lineage neurons including
355 the VMH only resulted in modest weight gain (Unger *et al.*, 2007). By contrast, deleting *Bdnf*
356 from Sim1-lineage neurons including the PVH resulted in a more severe obesity phenotype (An
357 *et al.*, 2015). This is consistent with the idea that Bdnf expression in PVH is critical for energy
358 homeostasis. We found that Rai1 expression in Bdnf-producing cells regulates energy
359 homeostasis in a sexually dimorphic manner. Specifically, female cKO mice showed normal
360 food intake, decreased energy expenditure, and reduced locomotor activity. In contrast, male
361 cKO mice showed increased food intake with no changes in locomotor activity. Intriguingly,
362 energy expenditure was increased in male cKO mice, likely due to the higher demand to
363 maintain normal activity levels in obese mice. In both sexes, cKO mice showed an increased fat
364 mass and adiposity with no change in lean mass, highlighting an important role for Rai1 in
365 regulating fat deposition. Our data also indicate that Bdnf-producing cells are only partially
366 responsible for obesity in SMS: male and female cKO mice become overweight by 15 weeks, in

367 contrast to SMS mice which become obese by 9 weeks of age, suggesting that non-Bdnf neurons
368 contribute to SMS phenotypes.

369 We found the metabolic phenotypes induced by deleting *Rai1* from Bdnf-producing cells were
370 specifically due to *Rai1* deletion in PVH^{Bdnf} neurons. Therefore, our study focused on PVH^{Bdnf}
371 neurons. Electrophysiological experiments showed that most wild-type PVH^{Bdnf} neurons display
372 high frequency spontaneous AP firing (1-10 Hz) at the resting membrane potential. The majority
373 of PVH^{Bdnf} neurons fire sharp APs held at a hyperpolarized potential and show repetitive
374 overshoot during the current ramp test. Loss of Rai1 significantly reduced intrinsic neuronal
375 excitability and increased inhibitory synaptic transmissions onto PVH^{Bdnf} neurons. Because
376 GABAergic Rai1 loss did not induce obesity (Huang *et al.*, 2016) and most Bdnf-producing
377 neurons are glutamatergic (Canals *et al*, 2001), the increased mIPSC amplitude was likely due to
378 postsynaptic changes in GABA receptor functions caused by Rai1 loss. The ionic changes in
379 PVH^{Bdnf} neurons that precisely explain these excitability changes await future investigations.
380 Different groups of PVH neurons show phasic bursting or slowly inactivating delayed rectifier
381 potassium conductance, which are properties mediated by different potassium channels (Lee *et*
382 *al.*, 2012). Given that our previous RNA-seq experiment found that hypothalamic Rai1 loss
383 induces misexpression of potassium channel subunits *Kcnc2* and *Kcnj11* (Huang *et al.*, 2016),
384 Rai1-dependent potassium channels are likely involved in altered neuronal activity. Furthermore,
385 we found fewer low threshold depolarization events in cKO PVH^{Bdnf} neurons during the
386 hyperpolarized voltage step, suggesting a potential involvement of HCN channels.

387 Our previous work found that Rai1 loss in the dentate gyrus resulted in neuronal
388 hyperexcitability (Chang *et al*, 2022b). Here we demonstrated that Rai1 loss in the hypothalamus
389 resulted in neuronal hypoactivity, suggesting that Rai1 regulates neuronal excitability in a cell

390 type-specific manner. Reduced PVH^{Bdnf} neuronal activity upon Rai1 loss could potentially
391 explain obesity, consistent with a previous report that found chemogenetic activation of PVH^{Bdnf}
392 neurons promotes negative energy balance by decreasing feeding and increasing energy
393 expenditure (Wu & Xu, 2022).

394 In future work, it would be interesting to dissect the sex-specific role of Rai1 in regulating the
395 functional development of PVH^{Bdnf} neurons. In addition to a role for Rai1 in regulating neuronal
396 activity, it is possible that Rai1 regulates other aspects of PVH^{Bdnf} neuronal function, including
397 projections to other brain regions to regulate energy homeostasis. In this regard, it would be
398 interesting to dissect how Rai1 controls circuit connectivity of PVH^{Bdnf} neurons and how Rai1
399 loss in PVH^{Bdnf} neurons affects nearby PVH^{TrkB} neurons that receive Bdnf signaling and are
400 linked to body weight regulation (An *et al*, 2020).

401 At the molecular level, our RPPA data show that *Rai1* depletion disrupted multiple intracellular
402 signalling pathways and resulted in the hypoactivation of specific phospho-signalling proteins.
403 Multiple early studies support the notion that Rai1 directly promotes Bdnf expression. First,
404 hypothalamic *Bdnf* mRNA levels were reduced in SMS mice (Burns *et al.*, 2010; Javed *et al.*,
405 2021) or mice with *Rai1* conditional deletions (Huang *et al.*, 2016). Second, Rai1 protein directly
406 binds to a promoter region of *Bdnf* (Huang *et al.*, 2016). Finally, when Rai1 expression was
407 induced using CRISPR activation, *Bdnf* mRNA levels were significantly elevated (Chang *et al*,
408 2022a).

409 To lend further support, here we show that SMS mice have reduced hypothalamic Bdnf protein
410 levels, as well as reduced activation of a TrkB downstream target Akt. Reduced Akt activity is
411 frequently associated with insulin resistance and obesity in mice (Shao *et al*, 2000) and children
412 (Su *et al.*, 2021). We also found that obesity, increased HDL levels, and insulin insensitivity in

413 SMS mice could be partially ameliorated using a small molecule drug (LM22A-4) that promotes
414 Akt phosphorylation. LM22A-4 penetrates the blood-brain barrier reasonably well and has been
415 shown to ameliorate symptoms of other neurological disorders associated with Bdnf dysfunction
416 including Rett syndrome, Huntington's disease, Dravet syndrome, and refractory neonatal
417 seizures (Canals *et al.*, 2004; Chang *et al.*, 2006; Gu *et al.*, 2022; Kron *et al.*, 2012; Ogier *et al.*,
418 2007). The partial rescue of SMS phenotypes that we observed contrasts with our previous
419 findings that found (1) AAV-mediated Bdnf overexpression in PVH at 3 weeks of age and (2)
420 genetically overexpressing Bdnf from early development could fully prevent the development of
421 obesity in SMS mice (Javed *et al.*, 2021). It is therefore possible that further increasing TrkB
422 signalling activation and/or earlier intervention might improve therapeutic outcomes.
423 Alternatively, our RPPA data showed that in addition to disruption of neurotrophin signalling,
424 multiple pathways including mTOR were downregulated in SMS. Increasing hypothalamic
425 mTOR activity has been shown to decrease food intake and body weight (Cota *et al.*, 2006).
426 Therefore, it is possible that enhancing both mTOR and TrkB signalling could achieve stronger
427 rescue of obesity in SMS mice. Nevertheless, these data support the concept that drugging TrkB
428 signalling may improve stereotypical repetitive behavior and partially alleviate metabolic
429 functions in a mouse model of SMS. Delayed symptom onset could provide a window of
430 opportunity for other interventions to further modify disease progression, an area requiring
431 further investigation.

432 This study has several limitations. First, whether the PVH^{Bdnf} neurons depend on Rai1 to regulate
433 adaptive thermogenesis awaits future analysis. It is known that a subset of posterior PVH^{Bdnf}
434 neurons project to the spinal cord and regulate thermogenesis (An *et al.*, 2015). However, we
435 found the weights of brown adipocytes were similar in control and cKO mice. Moreover, SMS

436 mice have normal respiratory exchange rate and there are currently no reports of defective
437 adaptive thermogenesis in SMS patients. This suggests that adaptive thermogenesis is not
438 impacted in SMS. Another limitation is that we did not test different doses, durations, and time
439 points for LM22A-4 treatment. The precise mechanisms by which LM22A-4 improves body
440 weight, metabolic function, and repetitive behaviours also remain unknown. Nevertheless, our
441 work identifies Rai1 as a novel regulator of the neuronal excitability of PVH^{Bdnf} neurons. This
442 regulation is critical for regulating food intake and energy expenditure. Our evidence suggests
443 that Bdnf-producing neurons are involved in SMS pathogenesis and that enhancing Bdnf-TrkB
444 signalling should be explored as a future therapeutic avenue for obesity and metabolic conditions
445 associated with reduced neurotrophin signalling (Xu & Xie, 2016).
446
447

448 **Materials and Methods**

449 **Animal Management**

450 The animal protocol was approved by the animal care committee of the Montreal General
451 Hospital and was performed according to the guidelines of the Canadian Council on Animal
452 Care. Mice were group-housed in 12-hour light/12-hour dark cycles with an *ad libitum* supply of
453 regular chow and water. The exception was in the fasting studies when the animals were food
454 deprived for 5 hours and in CALMS and food intake studies when animals were single-housed in
455 a 12-hour light/12-hour dark cycle with an *ad libitum* supply of regular chow and water. All mice
456 were maintained in a C57Bl/6J background. *Bdnf*$^{Cre/Cre}$, *Rosa-tomato*$^{td/td}$ (Ai9), and *Actβ*$^{Cre/Cre}$
457 mice were purchased from the Jackson laboratory. The *Rai1*$^{fl/fl}$ strain was previously generated
458 and characterized by us (Huang *et al.*, 2016). SMS mice (*Rai1*$^{+/-}$: whole-body germline *Rai1*
459 heterozygous knockout that genetically mimics SMS) were generated by crossing germline
460 *Actβ*$^{Cre/Cre}$ mice with *Rai1*$^{fl/+}$. To generate conditional knockout mice, *Bdnf*$^{Cre/+}$; *Rai1*$^{fl/+}$ mice
461 were crossed with *Rai1*$^{fl/+}$ to create control and experimental groups from the same littermate.

462

463 **Metabolic profiling**

464 Metabolic profiling was conducted in three different experimental conditions: male and female
465 conditional knockout mice, female virus-injected *Bdnf*$^{Cre/+}$ mice, and female drug- or saline-
466 injected SMS and control mice. Metabolic profiling included body weight and body composition
467 analysis, food intake measurement, indirect calorimetry for locomotion activity, energy
468 expenditure (EE), respiratory exchange rate (RER), measurement of serum lipids and leptin
469 levels, adipose tissue histology analysis, and glucose and insulin tolerance tests. All experiments

470 were performed as previously conducted experiments (Javed *et al.*, 2021). A brief description is
471 detailed below.

472

473 *Body weight and body composition analysis*

474 The body weight of animals was measured weekly from week 3 (weaning age) onward. Body
475 composition, including total fat and lean mass, were assessed using a nuclear EchoMRI whole-
476 body analyzer. Toward the end of experiments, animals were euthanized to collect brown
477 adipose, visceral, subcutaneous (inguinal) and ependymal white adipose tissues and weighed
478 using an analytical scale (Sartorius).

479

480 *Food Intake Measurement*

481 Mice were single-housed for food intake measurement. Food intake was measured over a one-
482 week period during which food was weighed prior to placement in the cage with minimal
483 bedding. Each morning remaining food inside the cage was weighed. The amount of total food
484 consumed was averaged over 7 days.

485

486 *Indirect Calorimetry*

487 A Comprehensive Lab Animal Monitoring System (CLAM) (Columbus instruments) was used to
488 measure the RER and EE (normalized over lean mass). Animals were singled-housed in the
489 CLAMS apparatus at 21˚C (70˚F) in a light–dark cycle matching their housing conditions for 24
490 hours (acclimation), followed by 48 hours of measurement.

491

492 *Serum lipid level determination*

493 A fluorescence-based assay kit (Abcam ab65390) was used to measure serum lipid levels. The
494 manufacturer's instructions were followed except that we used half-area black 96-well
495 microplates. Fluorescence measurements at 535/587 nm (Ex/Em) were recorded with the Ensight
496 instrument from PerkinElmer. A new standard curve ranging from 0 to 10 µg/ml was produced
497 for each microplate to accurately determine lipid levels in serum samples. Standards and samples
498 were loaded and analyzed twice.

499

500 *Histology of adipose tissue*

501 Ependymal white adipose tissues (WAT) were excised immediately after the animals were
502 euthanized and fixed with 10% formalin in PBS. The fixed tissues were dehydrated, embedded in
503 paraffin, and sectioned. Two 5-micrometre thick sections were taken from each animal and
504 stained with hematoxylin and eosin. Images of sections were then captured using an Aperio
505 ScanScope CS slide scanner at 20X optical magnification, and the resulting images were saved
506 in jpeg format using the ImageScope software. The images were manually cleaned to remove
507 non-adipose tissues such as lymph nodes. An automated method using the Adiposoft plugin
508 version 1.16 was utilized to determine adipocyte size and number from the jpeg images in Fiji
509 version 2.1.0/1.53c. The Adiposoft settings used excluded cells on edges and set a minimum and
510 maximum cell diameter of 20 and 300 µm, respectively. An experimental value of 2.49 µm per
511 pixel was determined using the Aperio scale bar and used for Adiposoft. To ensure accuracy, two
512 images from each animal were analyzed blindly, examining more than 1600 cells per mouse and

513 more than 9100 cells per condition. Adipocyte size frequencies were calculated using the
514 frequency function in Excel.

515

516 *Glucose and insulin tolerance tests*

517 For the glucose tolerance test, experimental mice were food deprived for 5 hours with *ad libitum*
518 water supply. A bolus of glucose (1.5g/kg of lean body weight) was then administered
519 intraperitoneally and glycemia was measured from tail vein blood samples using the Accu-chek
520 Performa glucometer at T0 (before the injection) as well as at 15, 30, 45, 60, 90 and 120 min
521 (after the injection). Tail vein blood samples were collected via a capillary for insulin assays at
522 T0, 15 and 30 min. For insulin tolerance tests, experimental mice were food-deprived for 5 hours
523 with *ad libitum* access to water. A bolus of insulin (1 U/kg of lean body weight) was
524 administered via an IP injection and glycemia was measured from blood sampled at the tail vein
525 using a Accu-chek Performa glucometer at T0 (before the injection), as well as at 15, 30, 45, 60,
526 90 and 120 min (after the injection). Tail vein blood samples were collected via a capillary for
527 insulin assays at T0.

528

529 **Stereotaxic Injections**

530 *Bdnf*$^{Cre/+}$ mice were anesthetized using isoflurane, and the ears were barred onto a stereotaxic
531 device (David Kopf Instruments). Adeno-associated viruses (AAVs, volume = 250 nl) were
532 bilaterally injected into the PVH using the following coordinates relative to the Bregma: -0.6 mm
533 anteroposterior (AP), ±0.35 mm mediolateral (ML) and -5.52 mm dorsoventral (DV). A
534 description of the AAV constructs and titre used is detailed below:

535 AAV9-CMV7-DIO-saCas9 (Viral title: >1 × 10^13), Vector Biolab

536 AAV9-CMV7-sgRai1-GFP (Viral title: >1 ×10^9), Applied Biological Materials Inc. Three
537 sgRNAs were pooled to target Rai1 (sgRNA1: TTCCTCGCCAGAGTAGCGCC, sgRNA2:
538 CCCAGCCTCATGATAGGCCG, sgRNA3: CCCAGCCTCATGATAGGCCG).

539

540 **Immunostaining of mouse brain tissues**

541 Immunostaining experiments were performed as previously described (Huang *et al*, 2012).
542 Briefly, mice were anesthetized and perfused with 1X PBS and 4% formaldehyde, and the brains
543 were dissected and fixed in 4% formaldehyde overnight. Fixed brains were then transferred to
544 30% sucrose solution and subsequently embedded in the OCT solution. The brains were then
545 sectioned (40µm), washed in PBS, permeabilized with 0.5% Triton X-100, and incubated with
546 10% normal donkey serum in PBS for 2 hours. The sections were then incubated overnight with
547 primary antibodies (Rai1: 1:500 dilution, RRID:AB_2921229 (Huang *et al.*, 2016); Bdnf: 1:500,
548 RRID:AB_10862052, Abcam ab108319; p-TrkB: 1:500 dilution, RRID:AB_2721199, Millipore
549 ABN1381; oxytocin: 1:1000 dilution, RRID:AB_11212999, Millipore MAB5296) at 4°C on a
550 shaker. The following day, sections were washed with 1X PBS twice for 10 minutes and
551 incubated with a secondary antibody (1:1000 dilution) for 3 hours at room temperature. Sections
552 were washed with 1X PBS once before mounting on glass slides with the DAPI-mounting
553 (DAPI-Fluoromount-G, SouthernBiotech) and then imaged using a confocal microscope
554 (Olympus FV-1000 confocal laser scanning microscope) with 20x or 40x objectives (NA 0.85
555 and 1.3, respectively). Z-stacks were taken with a step size of 1.0 µm with a 1024 x 1024
556 resolution. Images were acquired as a stack with at least 13 optical sections. Image analysis was
557 performed using the Fiji software.

558

559 **Real-Time Quantitative Reverse Transcription PCR (qRT-PCR)**

560 qRT-PCR was performed using mRNAs isolated from hypothalamic tissue samples. After
561 isolation of total RNA, mRNAs were reverse-transcribed with the SuperScript III First-Strand
562 Synthesis System (Thermo-Fisher). Quantitative PCR reactions were conducted using SsoFast
563 EvaGreen Supermix on a Bio-Rad qPCR system.

564

565 **Enzyme-linked immunosorbent assay (ELISA)**

566 ELISA was performed using hypothalamic tissues from 7-week-old SMS mice to assess the
567 mature Bdnf protein levels using a commercially available Bdnf ELISA kit (Mature BDNF
568 Rapid ELISA Kit: Human, Mouse, Rat).

569

570 **Western blotting analysis**

571 Mice were quickly decapitated, brains were rapidly removed, and hypothalamic tissues were
572 collected, weighed, and snap-frozen with liquid nitrogen. Hypothalamic tissues were lysed using
573 a tissue lysis buffer containing RIPA buffer (5M NaCl, 1M PH 8.0 Tris HCl, 1% NP.40, 10%
574 $C_{24}H_{39}NaO_4$, and 20% SDS) and the Halt™ Protease and Phosphatase Inhibitor Cocktail
575 (Thermo-Fisher). Lysates were first sonicated on ice for 15 seconds followed by centrifuging at
576 10000 RPM at 4°C for 10 minutes. The supernatant was collected in a separate Eppendorf tube,
577 and a BCA assay was performed to quantify protein levels. Proteins were then separated using
578 SDS-PAGE gel and transferred onto nitrocellulose membranes. To determine the

579 phosphorylation levels of Akt, membranes were cut and blocked in 5% milk in tris-buffered
580 saline (TBS) for 1 hour and then incubated overnight at 4°C with anti-p-Akt (Ser473) antibody
581 (1:1000 dilution, RRID:AB_2315049, Cell Signaling Technology 4060T) and anti-H3 antibody
582 (internal control: 1:1000 dilution, RRID:AB_302613, Abcam ab1791). The next day, membranes
583 were washed with TBST three times for five minutes before incubating with a HRP-conjugated
584 secondary antibody (1:10000 dilution, Thermo Fisher 200-403-095S). Membranes were later
585 stripped by incubating in 0.5M NaOH for 10 min and then re-probed for total Akt levels by
586 incubating with anti-Akt (C67E7) antibody (1:1000 dilution, Cell Signaling Technology 4691T).
587 The density of each immunoreactive phospho-protein band was expressed as a fraction of the
588 band for the total Akt protein in the same lane.

589

590 **Reverse-phase protein array (RPPA)**

591 Reverse-phase protein array (RPPA) was used for precise high-throughput quantification of total
592 and phospho-protein levels in different signalling pathways. Protein lysates from hypothalamic
593 tissues were extracted and transferred to 384-well microarray plates to print individual slides.
594 The slides were then labelled with validated antibodies that recognize total protein and specific
595 phosphorylation sites. SYPRO Ruby staining was used to measure total protein levels. The data
596 obtained from RPPA were normalized for individual samples. Each antibody's raw signal
597 intensity (SI) was determined by subtracting the background from the antibody-specific signals
598 during image analysis. The normalized antibody SI was expressed using the formula N = A - C/T
599 x M, where N is the normalized SI, A is the raw antibody SI, C is the negative control SI, T is the
600 SI of total protein, and M is the median SI of total protein from a spot within the same sample
601 group. Antibodies with SI less than 200 were filtered out, and quality control (QC) scores were

602 established to discard poor-quality reactions. The coefficient of variation (CV) score was
603 determined for each antibody and defined as the percentage of samples on a slide with a CV <
604 20%. Antibodies with a median technical triplicate CV >20% were also excluded from further
605 analysis. T-tests were performed for each antibody to identify differentially expressed proteins in
606 the SMS compared to control groups. PCA plots were generated for all samples, annotated with
607 their experimental group, and hierarchical clustering was performed using a Python analysis tool.
608 Enrichment analysis on the differentially expressed proteins was performed using an online data
609 resource string: version 11.5.

610

611 **Electrophysiology of acute brain slices**

612 Mouse brains were removed and placed in ice-cold carbonated slicing artificial cerebrospinal
613 fluid (aCSF), which contained (in mM) 124 NaCl, 3 KCl, 1.4 NaH_2PO_4, 26 $NaHCO_3$,1.3 Mg
614 SO4, 10 D-glucose, 0.5 $CaCl_2$, and 3.5 $MgCl_2$. Coronal sections (300 µm) were cut on a
615 vibratome. Slices were allowed to recover at 32 °C for 40 minutes and then at 30 °C for
616 30 minutes to 6 hours in the recording medium, carbonated aCSF (124 NaCl, 3 KCl, 1.4
617 NaH_2PO_4, 26 $NaHCO_3$,1.3 Mg SO4, 10 D-glucose, 2.4 $CaCl_2$, in mM, ~300 mOsm). Signals
618 were recorded with a 5× gain, low-pass filtered at 2 kHz, digitized at 10 kHz (Molecular
619 Devices Multiclamp 700B) and analyzed with pClamp 11 (Molecular Devices). Whole-cell
620 recordings were made using 3–5 MΩ pipettes filled with an internal solution that contained
621 (in mM) 131 potassium gluconate, 8 NaCl, 20 KCl, 2 EGTA, 10 HEPES, 2 MgATP and 0.3
622 Na3GTP (pH 7.2, with KOH, 300–310 mOsm with sucrose). For miniature current recording,
623 the internal solution contained (in mM) 130 gluconate acid, 8 CsCl, 1 NaCl, 2 EGTA, 0.8
624 CsOH, 10 HEPES, 2 MgATP and 0.3 Na3GTP (pH 7.2, with CsOH, 300–310 mOsm adjusted

625 with sucrose). mEPSCs were recorded in the presence of 1 μM TTX at a holding potential of -
626 70 mV. mIPSCs were recorded at a holding potential of +10 mV. The mIPSCs were analyzed
627 from events during a 2-minute continuous recording that contained > 15 events/neuron.
628 Additional calculations, statistical analysis, and plotting was performed in Microsoft Excel or
629 Prism (GraphPad).

630

631 **Spectrometric analysis of LM22A-4 levels in the brain**

632 We assessed the efficacy of LM22A-4, a small molecule pharmacological agent, in 8-week-old
633 SMS and control mice. LM22A-4, chemical name N1, N3, N5tris (2hydroxyethyl) 1, 3, 5
634 benzenetricarboxamide (Molecular formula: $C_{15}H_{21}N_3O_6$, Formula weight: 339.3), was
635 manufactured by Cayman Chemical with purity specification >98%. A stock solution was made
636 by first dissolving LM22A-4 in DMSO (solubility =30mg/ml) and then diluting it with 0.9%
637 isotonic sterilized saline solution (Sigma). To maximize brain concentrations, LM22A-4 was
638 administered both intranasally (5mg/kg) and intraperitoneally (50mg/kg), as previously reported
639 (Simmons *et al*, 2013). The bioavailability of this drug in the hypothalamus using these doses
640 and routes of administration was assessed with the reverse phase LC triple-quadrupole tandem
641 mass spectroscopic detection (LC-MS/MS) by Absorption Systems. Mice were euthanized, and
642 hypothalamic tissue was collected at either 1 h or 3 h post-injection (n= 4/timepoint). Known
643 amounts of LM22A-4 were added to the blank sample to generate a standard curve to verify test
644 accuracy.

645 **LM22A-4 treatment**

646 Mice were divided into four groups: Saline-injected control, Saline-injected SMS, LM22A-4-
647 injected SMS, and LM22A-4-injected control mice. Mice were injected daily, intra-nasally
648 (5mg/kg) and intraperitoneally (50mg/kg), for 7 weeks. Body weight was measured between 8
649 and 14 weeks of age. Food intake was measured from 14 to 15 weeks of age. After 15 weeks of
650 age, mice were euthanized to collect brown adipose, visceral, subcutaneous (inguinal) and
651 ependymal white adipose tissues and weighed using an analytical scale (Sartorius).
652 Hypothalamic brain tissues were collected for western blot analysis. Metabolic profiling was
653 performed on a separate cohort of mice injected for two weeks prior to the start of experiments
654 as well as at specific weeks during the experiment.

655

656 **Vertical rearing**

657 To measure vertical repetitive rearing, mice were taken into the testing room and allowed to
658 habituate for 1 h prior to testing. During the test, mice were placed in the center of a 45 cm (W)
659 × 45 cm (D) × 40 cm (H) square arena, and their movement was recorded for 10 minutes.

660

661 **Statistical analysis**

662 Sample sizes used were based on our previously studies (Huang *et al.*, 2016; Javed *et al.*, 2021).
663 The data were subjected to statistical analysis for significance by using GraphPad Prism 0.9.
664 Significance was defined as having a p-value < 0.05. The significance levels were expressed as
665 follows: * $p< 0.05$, ** $p<0.01$, *** $p<0.0001$, **** $p<0.0001$. The statistical tests used for each
666 analysis (e.g., Student's t-test, Fisher's exact test, analysis of variance [ANOVA]) are indicated
667 in the text and legends.

Data Availability

This study includes no data deposited in external repositories.

Acknowledgements

Sehrish Javed was supported by a doctoral award from the Fonds de Recherche du Québec - Santé (FRQS). This work was supported by the Rare Diseases: Models & Mechanisms Network and Smith-Magenis syndrome Research Foundation.

Author contributions

Sehrish Javed: Conceptualization; formal analysis; investigation; data curation; visualization; writing. **Ya-Ting Chang**: Formal analysis; investigation; data curation; visualization. **Yoobin Cho**: Formal analysis; investigation. **Yu-Ju Lee**: Formal analysis; investigation. **Hao-Cheng Chang**: Formal analysis; investigation. **Minza Haque**: Formal analysis; investigation. **Yu Cheng Lin**: Formal analysis; investigation. **Wei-Hsiang Huang**: Conceptualization; supervision; funding acquisition; visualization; writing; project administration.

Disclosure and competing interests statement

The authors do not have any conflicts of interest to disclose relating to this work.

References

Abad C, Cook MM, Cao L, Jones JR, Rao NR, Dukes-Rimsky L, Pauly R, Skinner C, Wang Y, Luo F *et al* (2018) A Rare De Novo RAI1 Gene Mutation Affecting BDNF-Enhancer-Driven Transcription Activity Associated with Autism and Atypical Smith-Magenis Syndrome Presentation. *Biology (Basel)* 7

Alaimo JT, Barton LV, Mullegama SV, Wills RD, Foster RH, Elsea SH (2015) Individuals with Smith-Magenis syndrome display profound neurodevelopmental behavioral deficiencies and exhibit food-related behaviors equivalent to Prader-Willi syndrome. *Res Dev Disabil* 47: 27-38

An JJ, Kinney CE, Tan JW, Liao GY, Kremer EJ, Xu B (2020) TrkB-expressing paraventricular hypothalamic neurons suppress appetite through multiple neurocircuits. *Nat Commun* 11: 1729

An JJ, Liao GY, Kinney CE, Sahibzada N, Xu B (2015) Discrete BDNF Neurons in the Paraventricular Hypothalamus Control Feeding and Energy Expenditure. *Cell Metab* 22: 175-188

Balthasar N, Dalgaard LT, Lee CE, Yu J, Funahashi H, Williams T, Ferreira M, Tang V, McGovern RA, Kenny CD *et al* (2005) Divergence of melanocortin pathways in the control of food intake and energy expenditure. *Cell* 123: 493-505

Boot E, Linders CC, Tromp SH, van den Boogaard MJ, van Eeghen AM (2021) Possible underreporting of pathogenic variants in RAI1 causing Smith-Magenis syndrome. *Am J Med Genet A* 185: 3167-3169

Burns B, Schmidt K, Williams SR, Kim S, Girirajan S, Elsea SH (2010) Rai1 haploinsufficiency causes reduced Bdnf expression resulting in hyperphagia, obesity and altered fat distribution in mice and humans with no evidence of metabolic syndrome. *Hum Mol Genet* 19: 4026-4042

Canals JM, Checa N, Marco S, Akerud P, Michels A, Perez-Navarro E, Tolosa E, Arenas E, Alberch J (2001) Expression of brain-derived neurotrophic factor in cortical neurons is regulated by striatal target area. *J Neurosci* 21: 117-124

Canals JM, Pineda JR, Torres-Peraza JF, Bosch M, Martin-Ibanez R, Munoz MT, Mengod G, Ernfors P, Alberch J (2004) Brain-derived neurotrophic factor regulates the onset and severity of motor dysfunction associated with enkephalinergic neuronal degeneration in Huntington's disease. *J Neurosci* 24: 7727-7739

Chang HC, Lee YJ, Javed S, Haque M, Chang YT, Lin YC, Oram C, Huang WH (2022a) rAAV-CRISPRa therapy corrects Rai1 haploinsufficiency and rescues selective disease features in Smith-Magenis syndrome mice. *J Biol Chem*: 102728

Chang Q, Khare G, Dani V, Nelson S, Jaenisch R (2006) The disease progression of Mecp2 mutant mice is affected by the level of BDNF expression. *Neuron* 49: 341-348

Chang YT, Kowalczyk M, Fogerson PM, Lee YJ, Haque M, Adams EL, Wang DC, DeNardo LA, Tessier-Lavigne M, Huguenard JR *et al* (2022b) Loss of Rai1 enhances hippocampal excitability and epileptogenesis in mouse models of Smith-Magenis syndrome. *Proc Natl Acad Sci U S A* 119: e2210122119

Collaboration NCDRF (2017) Worldwide trends in body-mass index, underweight, overweight, and obesity from 1975 to 2016: a pooled analysis of 2416 population-based measurement studies in 128.9 million children, adolescents, and adults. *Lancet* 390: 2627-2642

Colmers PLW, Bains JS (2018) Balancing tonic and phasic inhibition in hypothalamic corticotropin-releasing hormone neurons. *J Physiol* 596: 1919-1929

Cota D, Proulx K, Smith KA, Kozma SC, Thomas G, Woods SC, Seeley RJ (2006) Hypothalamic mTOR signaling regulates food intake. *Science* 312: 927-930

732 Edelman EA, Girirajan S, Finucane B, Patel PI, Lupski JR, Smith AC, Elsea SH (2007) Gender,
733 genotype, and phenotype differences in Smith-Magenis syndrome: a meta-analysis of 105 cases.
734 *Clin Genet* 71: 540-550
735 Gandhi AA, Wilson TA, Sisley S, Elsea SH, Foster RH (2022) Relationships between food-
736 related behaviors, obesity, and medication use in individuals with Smith-Magenis syndrome. *Res*
737 *Dev Disabil* 127: 104257
738 Gao H, Molinas AJR, Miyata K, Qiao X, Zsombok A (2017) Overactivity of Liver-Related
739 Neurons in the Paraventricular Nucleus of the Hypothalamus: Electrophysiological Findings in
740 db/db Mice. *J Neurosci* 37: 11140-11150
741 Garcia AD, Doan NB, Imura T, Bush TG, Sofroniew MV (2004) GFAP-expressing progenitors
742 are the principal source of constitutive neurogenesis in adult mouse forebrain. *Nat Neurosci* 7:
743 1233-1241
744 Gorski JA, Talley T, Qiu M, Puelles L, Rubenstein JL, Jones KR (2002) Cortical excitatory
745 neurons and glia, but not GABAergic neurons, are produced in the Emx1-expressing lineage. *J*
746 *Neurosci* 22: 6309-6314
747 Gray J, Yeo GS, Cox JJ, Morton J, Adlam AL, Keogh JM, Yanovski JA, El Gharbawy A, Han JC,
748 Tung YC *et al* (2006) Hyperphagia, severe obesity, impaired cognitive function, and
749 hyperactivity associated with functional loss of one copy of the brain-derived neurotrophic factor
750 (BDNF) gene. *Diabetes* 55: 3366-3371
751 Gu F, Parada I, Yang T, Longo FM, Prince DA (2022) Chronic partial TrkB activation reduces
752 seizures and mortality in a mouse model of Dravet syndrome. *Proc Natl Acad Sci U S A* 119
753 Huang WH, Guenthner CJ, Xu J, Nguyen T, Schwarz LA, Wilkinson AW, Gozani O, Chang HY,
754 Shamloo M, Luo L (2016) Molecular and Neural Functions of Rai1, the Causal Gene for Smith-
755 Magenis Syndrome. *Neuron* 92: 392-406
756 Huang WH, Tupal S, Huang TW, Ward CS, Neul JL, Klisch TJ, Gray PA, Zoghbi HY (2012)
757 Atoh1 governs the migration of postmitotic neurons that shape respiratory effectiveness at birth
758 and chemoresponsiveness in adulthood. *Neuron* 75: 799-809
759 Huang WH, Wang DC, Allen WE, Klope M, Hu H, Shamloo M, Luo L (2018) Early adolescent
760 Rai1 reactivation reverses transcriptional and social interaction deficits in a mouse model of
761 Smith-Magenis syndrome. *Proc Natl Acad Sci U S A*
762 Javed S, Lee YJ, Xu J, Huang WH (2021) Temporal dissection of Rai1 function reveals brain-
763 derived neurotrophic factor as a potential therapeutic target for Smith-Magenis syndrome. *Hum*
764 *Mol Genet* 31: 275-288
765 Javed S, Selliah T, Lee YJ, Huang WH (2020) Dosage-sensitive genes in autism spectrum
766 disorders: From neurobiology to therapy. *Neurosci Biobehav Rev* 118: 538-567
767 Kron M, Howell CJ, Adams IT, Ransbottom M, Christian D, Ogier M, Katz DM (2012) Brain
768 activity mapping in Mecp2 mutant mice reveals functional deficits in forebrain circuits,
769 including key nodes in the default mode network, that are reversed with ketamine treatment. *J*
770 *Neurosci* 32: 13860-13872
771 Lee SK, Lee S, Shin SY, Ryu PD, Lee SY (2012) Single cell analysis of voltage-gated potassium
772 channels that determines neuronal types of rat hypothalamic paraventricular nucleus neurons.
773 *Neuroscience* 205: 49-62
774 Loos RJF, Yeo GSH (2022) The genetics of obesity: from discovery to biology. *Nat Rev Genet*
775 23: 120-133

776 Massa SM, Yang T, Xie Y, Shi J, Bilgen M, Joyce JN, Nehama D, Rajadas J, Longo FM (2010)
777 Small molecule BDNF mimetics activate TrkB signaling and prevent neuronal degeneration in
778 rodents. *J Clin Invest* 120: 1774-1785
779 Moss J, Oliver C, Arron K, Burbidge C, Berg K (2009) The prevalence and phenomenology of
780 repetitive behavior in genetic syndromes. *J Autism Dev Disord* 39: 572-588
781 Ogier M, Wang H, Hong E, Wang Q, Greenberg ME, Katz DM (2007) Brain-derived
782 neurotrophic factor expression and respiratory function improve after ampakine treatment in a
783 mouse model of Rett syndrome. *J Neurosci* 27: 10912-10917
784 Rao NR, Abad C, Perez IC, Srivastava AK, Young JI, Walz K (2017) Rai1 Haploinsufficiency Is
785 Associated with Social Abnormalities in Mice. *Biology (Basel)* 6
786 Schultze SM, Hemmings BA, Niessen M, Tschopp O (2012) PI3K/AKT, MAPK and AMPK
787 signalling: protein kinases in glucose homeostasis. *Expert Rev Mol Med* 14: e1
788 Shao J, Yamashita H, Qiao L, Friedman JE (2000) Decreased Akt kinase activity and insulin
789 resistance in C57BL/KsJ-Leprdb/db mice. *J Endocrinol* 167: 107-115
790 Simmons DA, Belichenko NP, Yang T, Condon C, Monbureau M, Shamloo M, Jing D, Massa
791 SM, Longo FM (2013) A small molecule TrkB ligand reduces motor impairment and
792 neuropathology in R6/2 and BACHD mouse models of Huntington's disease. *J Neurosci* 33:
793 18712-18727
794 Slager RE, Newton TL, Vlangos CN, Finucane B, Elsea SH (2003) Mutations in RAI1
795 associated with Smith-Magenis syndrome. *Nat Genet* 33: 466-468
796 Smith AC, McGavran L, Robinson J, Waldstein G, Macfarlane J, Zonona J, Reiss J, Lahr M,
797 Allen L, Magenis E (1986) Interstitial deletion of (17)(p11.2p11.2) in nine patients. *Am J Med*
798 *Genet* 24: 393-414
799 Su X, Gu D, Xu L, Liang Z, Luo X, Yang P, Yang J (2021) PI3K/Akt pathway expression in
800 children with different obesity degrees and its relationship with glucolipid metabolism and
801 insulin resistance. *Am J Transl Res* 13: 6592-6598
802 Tan CL, Cooke EK, Leib DE, Lin YC, Daly GE, Zimmerman CA, Knight ZA (2016) Warm-
803 Sensitive Neurons that Control Body Temperature. *Cell* 167: 47-59 e15
804 Taniguchi H, He M, Wu P, Kim S, Paik R, Sugino K, Kvitsiani D, Kvitsani D, Fu Y, Lu J *et al*
805 (2011) A resource of Cre driver lines for genetic targeting of GABAergic neurons in cerebral
806 cortex. *Neuron* 71: 995-1013
807 Unger TJ, Calderon GA, Bradley LC, Sena-Esteves M, Rios M (2007) Selective deletion of Bdnf
808 in the ventromedial and dorsomedial hypothalamus of adult mice results in hyperphagic behavior
809 and obesity. *J Neurosci* 27: 14265-14274
810 Wu SW, Xu B (2022) Rapid and Lasting Effects of Activating BDNF-Expressing PVH Neurons
811 on Energy Balance. *eNeuro* 9
812 Xu B, Goulding EH, Zang K, Cepoi D, Cone RD, Jones KR, Tecott LH, Reichardt LF (2003)
813 Brain-derived neurotrophic factor regulates energy balance downstream of melanocortin-4
814 receptor. *Nat Neurosci* 6: 736-742
815 Xu B, Xie X (2016) Neurotrophic factor control of satiety and body weight. *Nat Rev Neurosci*
816 17: 282-292
817 Xu Y, Lu Y, Cassidy RM, Mangieri LR, Zhu C, Huang X, Jiang Z, Justice NJ, Xu Y, Arenkiel BR
818 *et al* (2019) Identification of a neurocircuit underlying regulation of feeding by stress-related
819 emotional responses. *Nat Commun* 10: 3446

820 Yeo GS, Connie Hung CC, Rochford J, Keogh J, Gray J, Sivaramakrishnan S, O'Rahilly S,
821 Farooqi IS (2004) A de novo mutation affecting human TrkB associated with severe obesity and
822 developmental delay. *Nat Neurosci* 7: 1187-1189

823

824

825

826 **Figures and Figure legends**

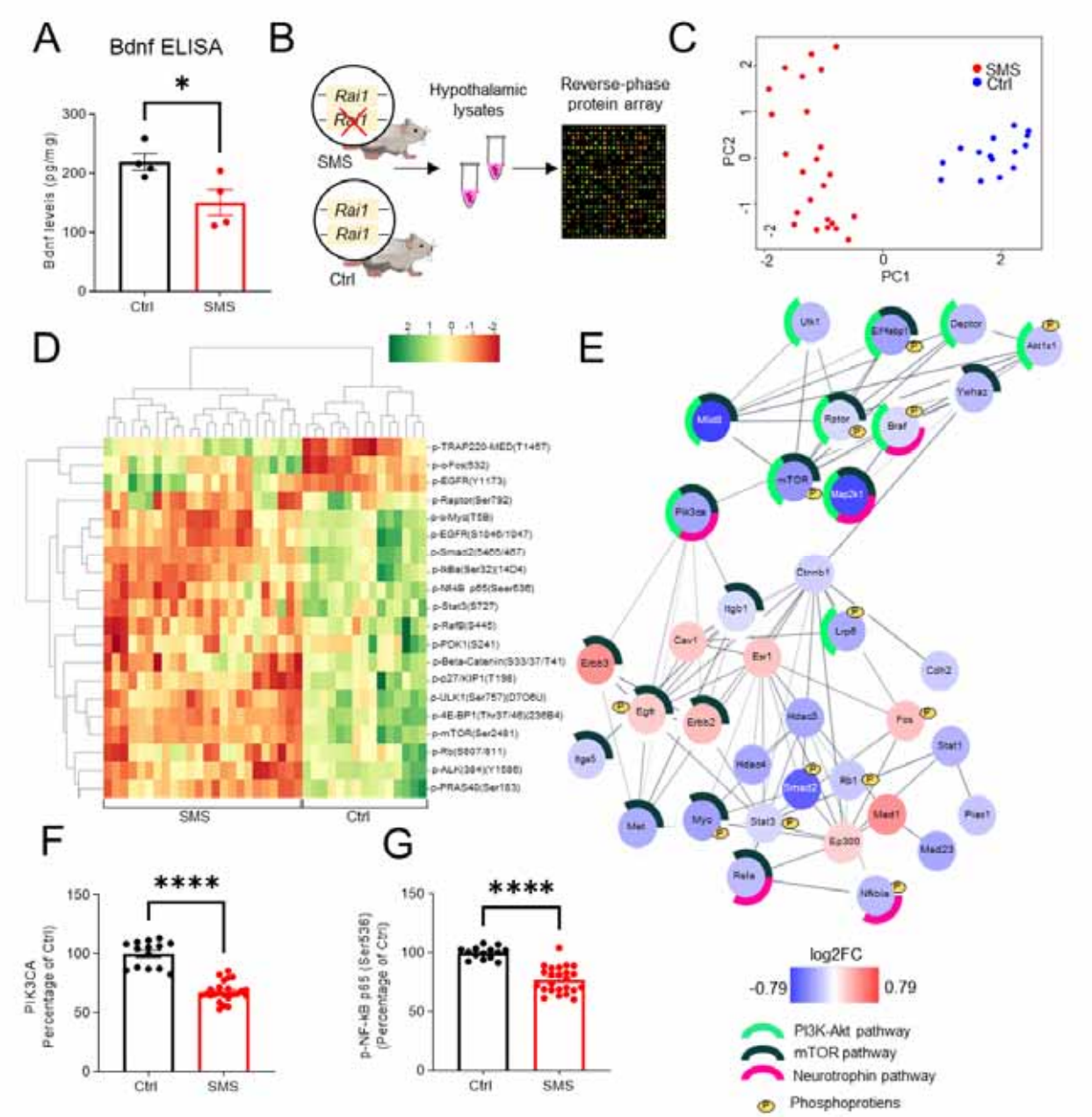

827

828 **Figure 1: *Rai1* haploinsufficiency disrupts hypothalamic proteomic profile in mice**

829 **(A)** ELISA showing that Bdnf protein levels in hypothalamic tissues were significantly reduced
830 in SMS mice compared to controls (n=4/genotype). *p<0.05, student's t-test.

831 **(B)** A schematic diagram showing the experimental strategy. Hypothalamic tissue lysates from 7-
832 week-old control (n = 5, 3 technical triplicates/sample) and SMS (n=8, 3 technical

833 triplicates/sample) mice were subjected to RPPA that utilizes a cocktail of 240 validated
834 antibodies to probe several key intracellular signalling pathways by quantifying the expression
835 levels of total and phosphorylated proteins

836 **(C)** Principal component analysis segregates the SMS and Ctrl groups where PC1 explains 47%
837 of the variance, and PC2 explains 25% of the variance.

838 **(D)** Heat map showing hierarchical clustering of differentially expressed phospho-proteins: most
839 showed reduced levels in SMS samples.

840 **(E)** Protein-protein interaction (PPI) analysis showing differentially expressed proteins and
841 phospho-proteins in a crosstalk network. PPI enrichment p-value: < 1.0e-16. The nodes represent
842 the proteins/phospho-proteins and the lines indicate physical interactions. Associations with
843 specific molecular pathways are indicated as color coded outer rings.

844 **(F-G)** Protein levels of two neurotrophin pathway-related nodes, PIK3CA **(F)** and phospho-NF-
845 kB **(G)**, which were significantly reduced in SMS samples. ****p<0.0001, student's t-test.

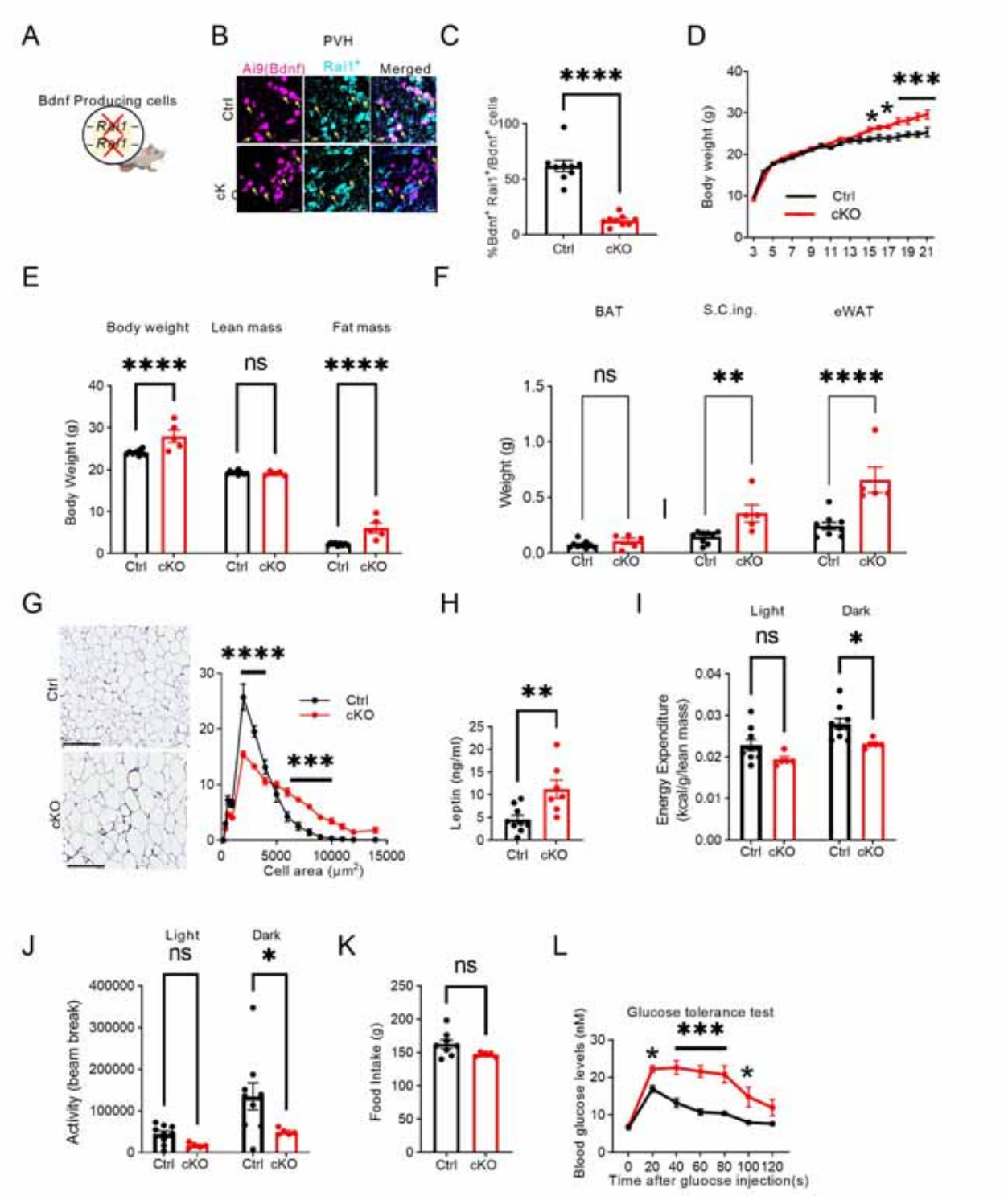

Figure 2: Rai1 is required in Bdnf-producing cells to regulate energy metabolism

(A) A schematic diagram showing selective deletion of *Rai1* from Bdnf-producing cells in mice.

849 **(B)** Representative images showing that in Ctrl mice (*Bdnf*$^{Cre/+}$; *Ai9*), many PVH^{Bdnf} neurons
850 (magenta) express Rai1 (cyan, double-positive cells were indicated with yellow arrowheads). By
851 contrast, PVH^{Bdnf} neurons lack Rai1 expression in the cKO group (yellow arrowheads)
852 (*Bdnf*$^{Cre/+}$; *Rai1*$^{fl/fl}$; *Ai9*). Scale bars = 20µm.

853 **(C)** Percentage of PVH^{Bdnf} neurons co-expressing Rai1 in Ctrl (n=3) and cKO (n=3) mice.
854 ****p<0.0001, student's t-test.

855 **(D)** Female cKO mice (n = 12) showed a significant weight gain when compared to female Ctrl
856 mice (n = 10).

857 **(E)** Body composition was measured with Echo-MRI, showing an increased fat mass in 26-
858 week-old mice.

859 **(F)** Fat mass of brown adipocytes (BAT), subcutaneous inguinal (S.C.ing) and epididymal white
860 adipose tissue (eWAT) in Ctrl and cKO mice.

861 **(G)** Representative images showing eWAT adipocyte hypertrophy of the cKO mice (left). Scale
862 bar = 500µm. Frequency distribution of adipocytes at each cellular size (right).

863 **(H)** Female cKO mice showed significantly increased blood leptin levels.

864 **(I)** Female cKO mice showed reduced energy expenditure during the dark phase. ns indicates not
865 significantly different.

866 **(J)** Female cKO mice showed reduced locomotor activity during the dark phase. ns indicates
867 difference is not significant.

868 **(K)** Female cKO mice showed similar food intake as control mice. ns indicates not significant.

869 **(L)** Glucose tolerance test showing that cKO mice became hyperglycemic 20 minutes after
870 intraperitoneal glucose administration, suggesting glucose intolerance.

871 Data are shown as mean±SEM. Statistics for **D-G**, **I-J**, **L**: ns indicates not significantly different,
872 *p<0.05, **p < 0.01, ***p<0.001, ****p < 0.0001, one or two-way ANOVA with Šidák's
873 multiple comparisons test.

874

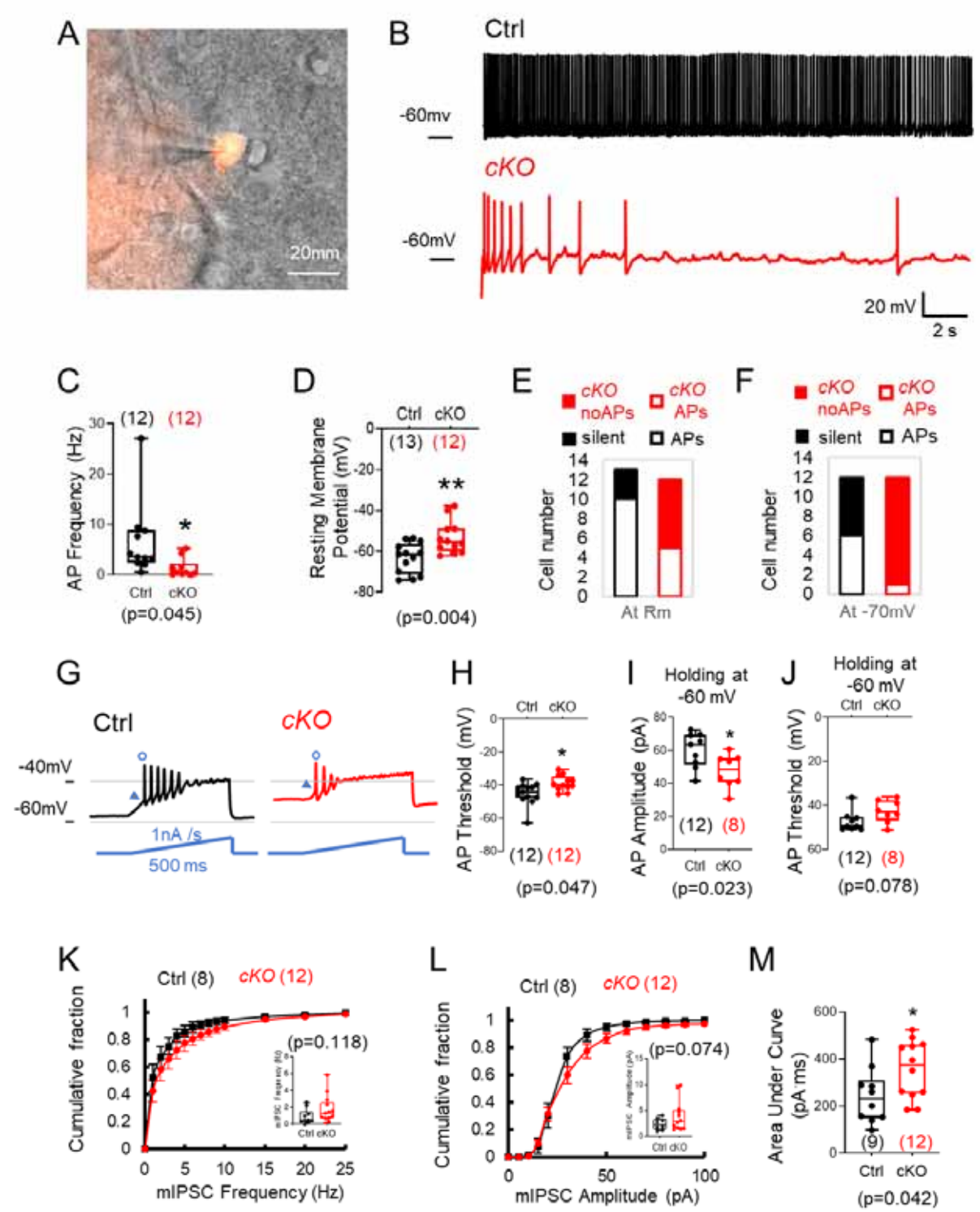

875

876 **Figure 3: Rai1 loss reduces intrinsic neuronal excitability and enhances inhibitory synaptic**

877 **transmission of PVH^{Bdnf} neurons**

878 **(A)** A representative image showing a patched PVH^{Bdnf} neuron labelled by *Bdnf*^{Cre}-dependent
879 tdTomato fluorescence signals.

880 **(B-C)** Representative traces of spontaneous firing of control (black) and cKO (red) neurons at a
881 holding voltage of -60mV **(B)**. The average spontaneous AP firing frequencies are shown in **(C)**.

882 **(D)** The resting membrane potentials of control (black) and cKO (red) PVH^{Bdnf} neurons.

883 **(E-F)** The number of control (black) and cKO (red) PVH^{Bdnf} neurons that showed spontaneous
884 firing (solid) or are silent (open) at resting membrane potentials **(e)** and at a holding voltage of -
885 70mV **(f)**.

886 **(G)** Representative traces of elicited APs in control (black) and cKO (red) PVH^{Bdnf} neurons
887 responding to an inject current (bottom, blue), which ramps up from the resting membrane
888 potentials at 1 nA per second for 500ms.

889 **(H)** The threshold of the first AP initiated by a current ramp in control (black) and cKO (red)
890 PVH^{Bdnf} neurons.

891 **(I-J)** The amplitude **(I)** and threshold **(J)** for the first AP firing at the holding voltage of -60mV
892 in control (black) and cKO (red) PVH^{Bdnf} neurons.

893 **(K)** The cumulative fractions of mIPSC frequency measured in control (black) and cKO(red)
894 PVH^{Bdnf} neurons. The average frequency of events from a 2-min stable recording of each neuron
895 is shown in the inset.

896 **(L)** The cumulative fractions of mIPSC amplitude of control (black) and cKO (red) PVH^{Bdnf}
897 neurons. The average amplitude of events from a 2-min stable recording of each neuron is
898 normalized to its capacitance and shown in the inset.

899 **(M)** The area under the curve of each mIPSC event from a 2-min recording is averaged. Controls
900 are shown in black, and cKOs are shown in red.

901 Data are shown as mean±SEM. Statistics: Neuron numbers are in brackets (more than 3
902 mice/genotype); *$p<0.05$, unpaired student's t-tests.

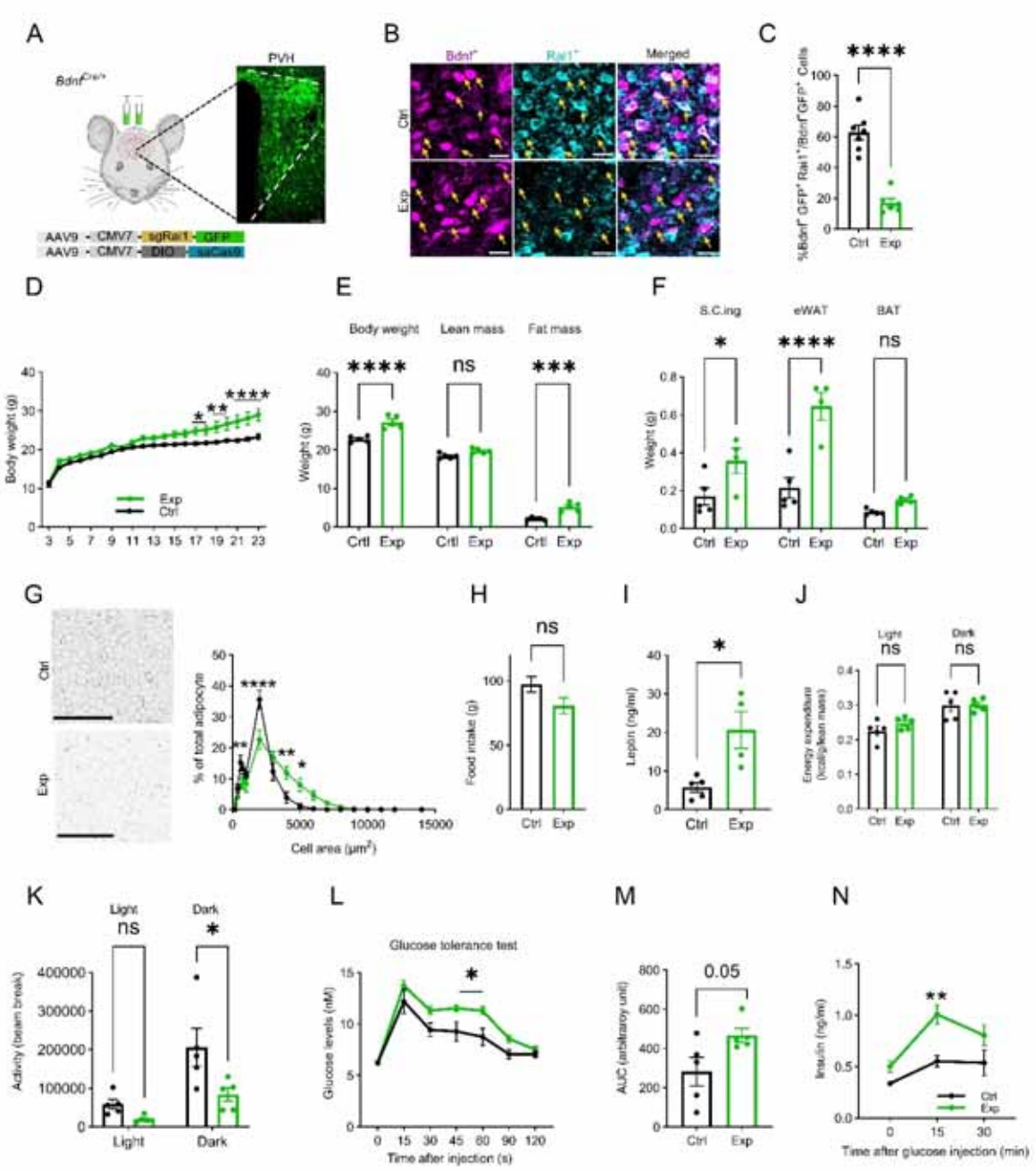

903

904 **Figure 4: Selective *Rai1* ablation in PVH^{Bdnf} neurons induces obesity**

905 **(A)** A schematic showing stereotaxic injection of adeno-associated viruses (AAVs) expressing
906 Cas9 protein and single-guide RNAs targeting Rai1 (sgRai1) to delete *Rai1* from the PVH^{Bdnf}
907 neurons of *Bdnf*$^{Cre/+}$ female mice. Scale bar = 50μm.

908 **(B)** Representative images showing that Rai1 immunoreactivity (cyan) was dramatically reduced
909 in *Bdnf*$^{Cre/+}$*; Ai9* mice injected with both sgRai1 and DIO-saCas9 viruses (Exp group, bottom
910 row) into the PVH. In contrast, many PVH^{Bdnf} neurons in *Bdnf*$^{Cre/+}$*; Ai9* mice injected only with
911 the sgRai1 virus showed Rai1 expression (Ctrl group, top row).

912 **(C)** The percentage of PVH^{Bdnf} neurons co-expressing Rai1 and GFP (virus) was significantly
913 reduced in the Exp group, indicating a successful *Rai1* deletion.

914 **(D)** PVH^{Bdnf} neuron-specific *Rai1* deletion induced body weight gain in Exp mice.

915 **(E)** Body composition was measured with Echo-MRI, showing an increased fat mass deposition
916 in 26-week-old Exp mice.

917 **(F)** Fat deposition analysis shows that the Exp group has significantly more subcutaneous
918 inguinal (S.C.ing) and epididymal white adipose tissue (eWAT) mass (grams). ns indicates not
919 significantly different.

920 **(G)** Representative images showing eWAT adipocyte hypertrophy of the Exp group (left). Scale
921 bar = 500µm. Frequency distribution of adipocytes at each cellular size (right). ns indicates not
922 significantly different.

923 **(H)** Exp and control mice showed similar food intake. ns indicates not significant, student's t-
924 test.

925 **(I)** Blood leptin levels were significantly increased in the Exp mice. *$p<0.05$, student's t-test.

926 **(J)** Exp and control mice showed similar energy expenditure.

927 **(K)** Exp mice showed reduced locomotor activity in the dark phase.

928 **(L)** Exp mice became hyperglycemic during the glucose tolerance test.

929 **(M)** Measurement of the area under the curve (AUC) in Exp and Ctrl mice during the glucose
930 tolerance test. $p = 0.0522$, student's t-test.

931 **(N)** Exp mice showed increased plasma insulin levels during the glucose tolerance test.

Data are shown as mean±SEM. Statistics for **C-G**, **J-L**, **N**: ns indicates not significantly different, *$p<0.05$, **$p < 0.01$, ***$p<0.001$, ****$p < 0.0001$, one or two-way ANOVA with Šidák's multiple comparisons test.

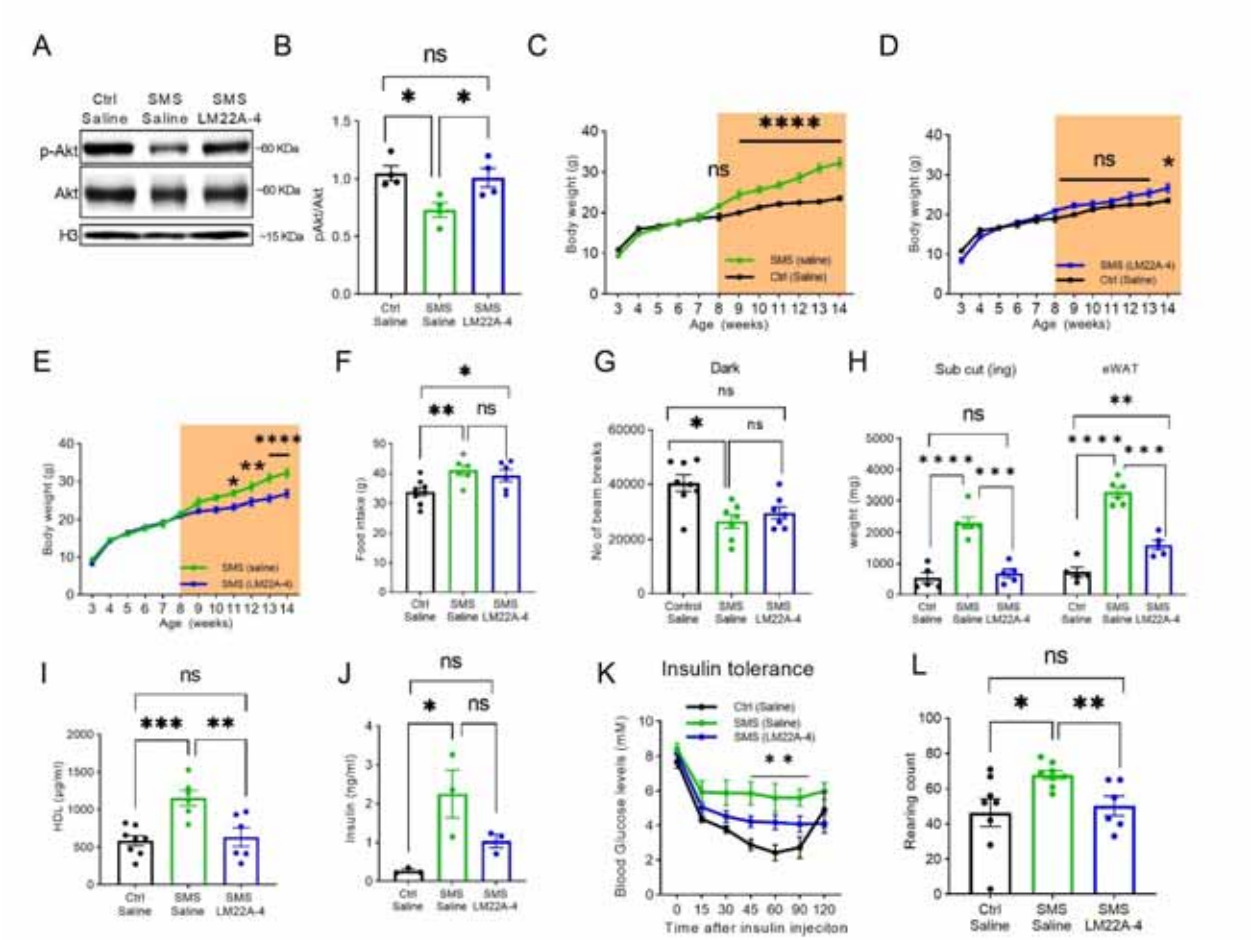

Figure 5: LM22A-4 treatment partially alleviates obesity and stereotypic behaviour in adult SMS mice

(A) Representative western blot showing p-Akt, total Akt, Histone 3 (H3, a loading control) levels in the hypothalamus of saline-treated Ctrl, saline-treated SMS and LM22A-4-treated SMS mice.

(B) Quantification showing phosphorylation deficits in Akt protein levels of the hypothalamus were reversed by LM22A-4 treatment in SMS mice.

(C-E) Body weight of saline-injected control, saline-injected SMS, and LM22A-4 injected SMS mice. Saline or LM22A-4 treatment periods were highlighted in orange. Ns indicates not significantly different.

(F) Food intake (in grams) of saline-injected control, saline-injected SMS, and LM22A-4 injected SMS mice.

949 **(G)** Locomotor activity (number of beam breaks) for saline-injected control, saline-injected
950 SMS, and LM22A-4 injected SMS mice.

951 **(H)** Fat deposition analysis showing that the saline-injected SMS group has significantly more
952 subcutaneous inguinal (S.C.ing) and epididymal white adipose tissue (eWAT) mass (grams) than
953 saline-injected Ctrl mice. S.C.ing and eWAT mass in LM22A-4 injected mice is comparable to
954 the saline-injected mice.

955 **(I)** Insulin tolerance test performed on saline-injected control, saline-injected SMS, and LM22A-
956 4 injected SMS mice, two-week post daily administration of LM22A-4 or saline, shows
957 reductions in the blood glucose levels of LM22A-4 treated SMS mice. * Shows significance
958 between saline injected Ctrl and saline injected SMS group.

959 **(J)** Insulin levels in saline-injected control, saline-injected SMS, and LM22A-4 injected SMS
960 mice right before the start of insulin tolerance test (time point 0).

961 **(K)** High density lipoprotein (HDL) levels were restored to normal in LM22A-4 injected SMS
962 mice.

963 **(L)** Stereotypic rearing behaviour was fully rescued in LM22A-4 treated SMS mice.

964 Data are shown as mean±SEM. Statistics for **B-L**: ns indicates not significantly different,
965 *$p<0.05$, **$p < 0.01$, ***$p<0.001$, ****$p < 0.0001$, one or two-way ANOVA with Šidák's
966 multiple comparisons test.

967

968

969

970

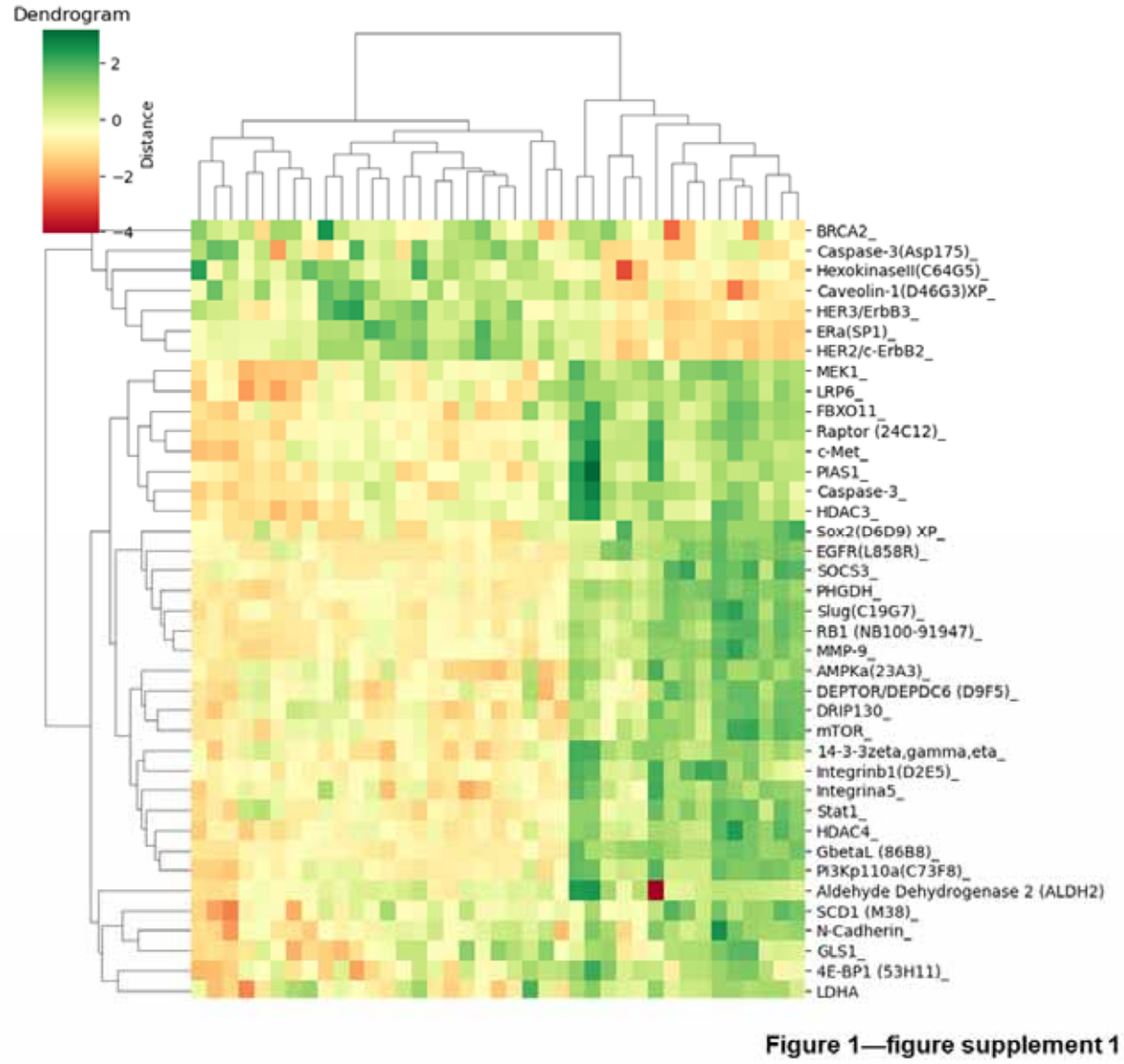

Fig 1-figure supplement 1: Differentially expressed proteins in the hypothalamus of SMS mice

A heat map showing hierarchical clustering of differentially expressed proteins in the hypothalamus of SMS mice.

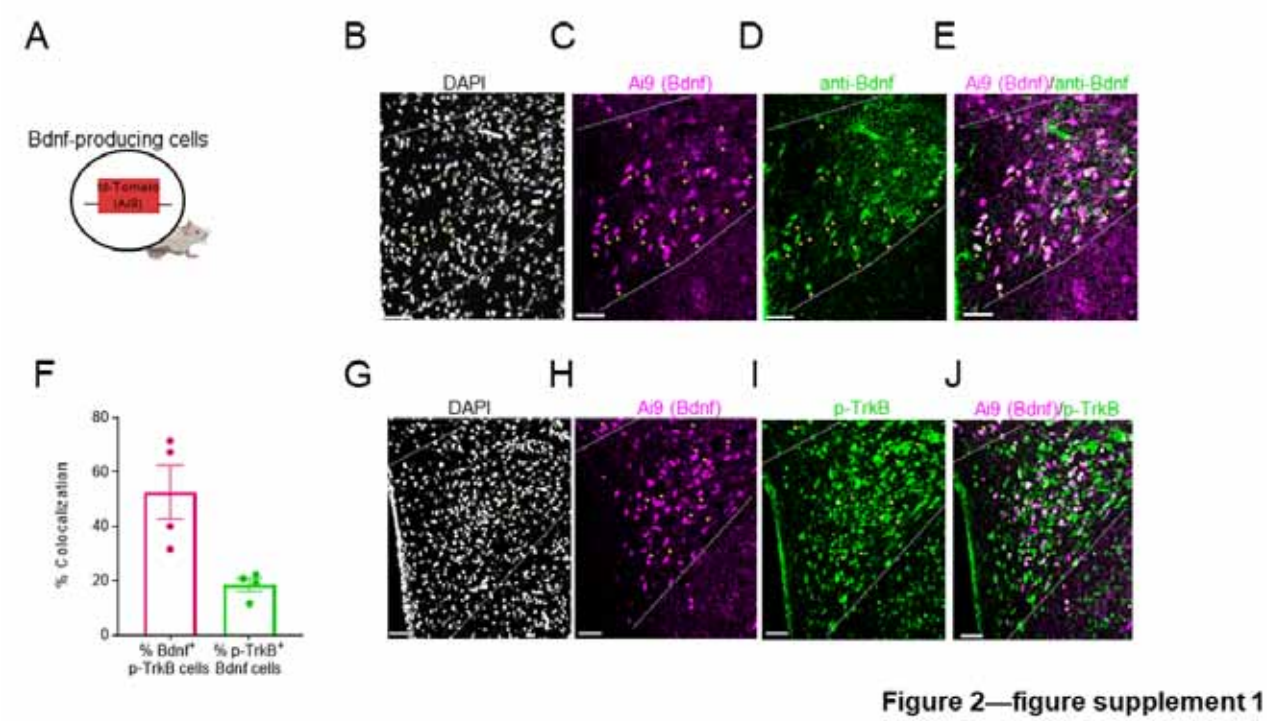

Fig 2-figure supplement 1: The *Bdnf*^{Cre} allele labels Bdnf-producing neurons in the paraventricular nucleus of hypothalamus

(A) Schematic showing a transgenic mouse expressing *Bdnf*^{Cre}-dependent td-Tomato (Ai9) signals in Bdnf-expressing cells.

(B-E) Colocalization of *Bdnf*^{Cre}-dependent td-Tomato signals with endogenous Bdnf protein. Black: DAPI, Magenta: Bdnf-producing cells, Green: endogenously Bdnf. Scale bar: 50 µm.

(F) Quantification showing the percentage of Bdnf-producing cells that express p-TrkB protein (left bar, magenta) and the percentage of p-TrkB-expressing cells that express Bdnf (right bar, green) in the PVH. Data are shown as mean±SEM.

(H-J) Representative images showing that Bdnf-producing cells and p-TrkB signals are colocalized in the PVH. Black: DAPI, Magenta: Bdnf-producing cells, Green: phospho-TrkB^{816} (Scale bar: 50µm).

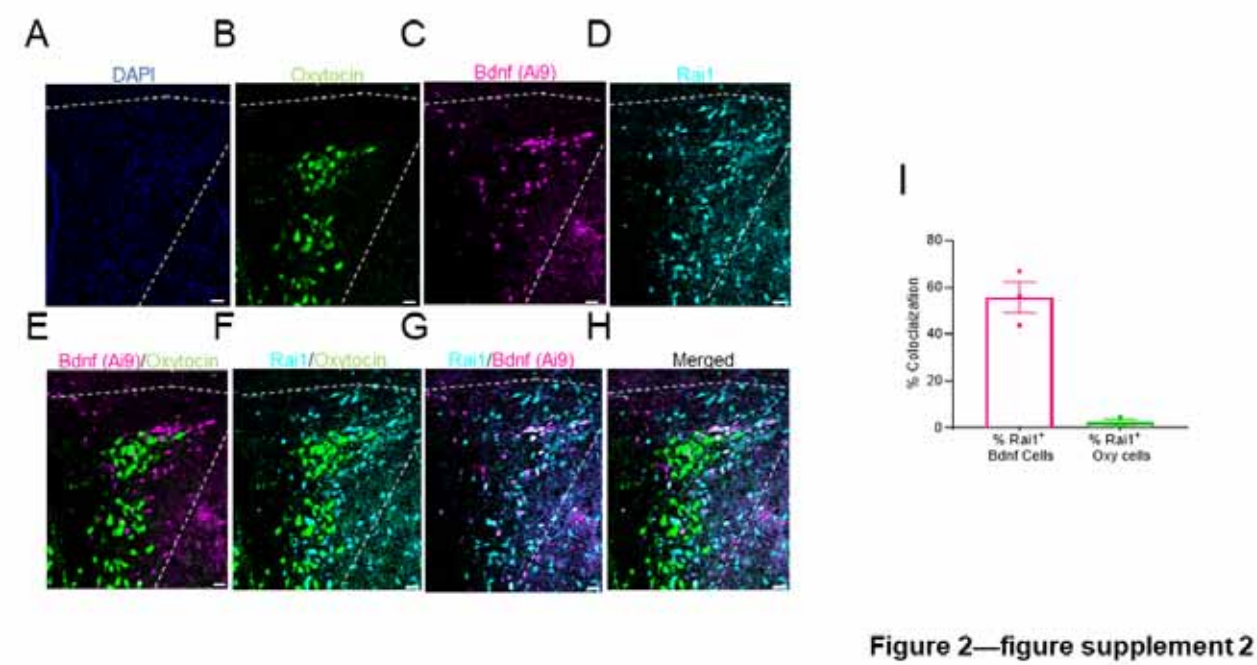

Fig 2-figure supplement 2: Rai1 expression in Bdnf-expressing but not oxytocin-expressing magnocellular PVH neurons

(A-H) Representative images DAPI expression (blue, **A**), oxytocin (green, **B**), Bdnf-producing cells (Ai9 reporter, magenta, **C**), and Rai1 protein (cyan, **D**) in the PVH. Note that Bdnf-producing neurons are distinct from the oxytocin-expressing neurons (**E**) and that Rai1 is more selectively expressed in the Bdnf-expressing neurons (**F-H**).

(I) Quantification showing the percentage of Rai1^{+} cells that co-express either Bdnf (left bar, magenta) or oxytocin (right bar, green) in the PVH. n=3 mice/group. Data are shown as mean±SEM.

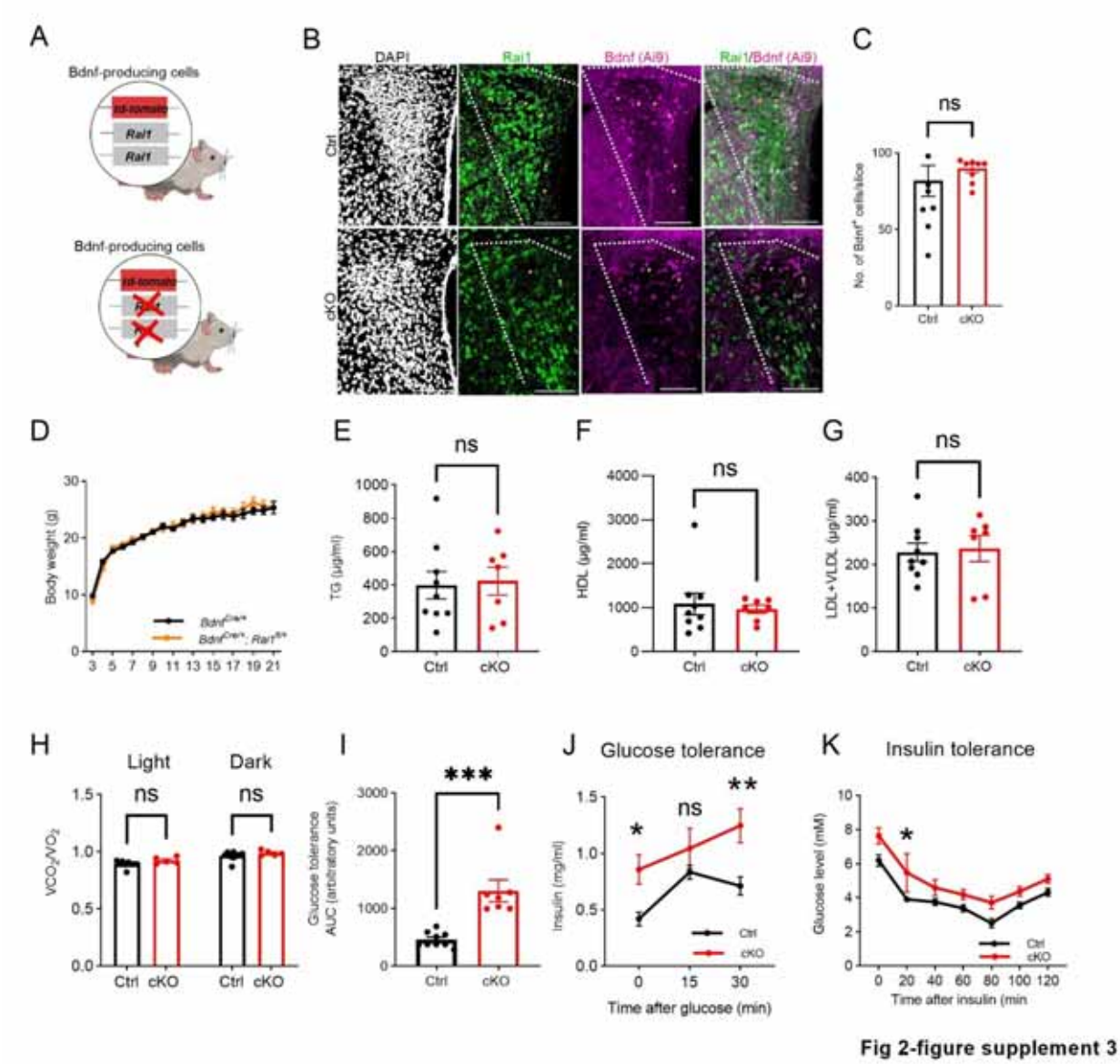

Fig 2-figure supplement 3: Ablating *Rai1* from the Bdnf-producing cells induces body weight gain and defective energy homeostasis

(A) Schematic representation of the conditional knockout mice carrying either normal Rai1 alleles and the Ai9 reporter in Bdnf-producing cells (top) or homozygous *Rai1* deletion and the Ai9 reporter in the Bdnf-producing cells.

(B) Representative images showing the expression of DAPI (white), Rai1-expressing cells (green), and Bdnf-expressing cells (Ai9 reporter, magenta) in the PVH. The top panel shows the Ctrl group with Rai1-Ai9 co-expression (yellow arrowheads) and the bottom panel shows

1014 reduced Rai1 and Ai9 colocalization (yellow arrowheads). Note that Rai1 expression was still
1015 detected in non-Bdnf neurons in the PVH.

1016 **(C)** Quantification showing the percentage of Bdnf-producing cells was not altered by *Rai1*
1017 deletion, indicating that Rai1 loss did not impair the generation or survival of PVH^{Bdnf} neurons.
1018 ns indicates not significantly different, student's t-test.

1019 **(D)** The $Bdnf^{Cre/+}$ and $Bdnf^{Cre/+}$; $Rai1^{fl/+}$ female mice had similar body weights.

1020 **(E-G)** Blood parameter analysis of triglycerides (TG), high-density lipoprotein (HDL), low-
1021 density lipoprotein and very low-density lipoprotein (LDL+VLDL) did not differ between Ctrl
1022 and cKO mice. ns indicates not significantly different, student's t-test.

1023 **(H)** Respiratory exchange rate did not differ between Ctrl and cKO mice.

1024 **(I)** In the glucose tolerance test, the cKO mice showed an increased area under curve (AUC).
1025 ***p<0.001, student's t-test.

1026 **(J)** In the glucose tolerance test, cKO mice showed increased insulin levels at the beginning of
1027 the test and at 30 minutes after glucose administration.

1028 **(K)** In the insulin tolerance test, blood glucose level after insulin injection.

1029 Data are shown as mean±SEM. Statistics for **D**, **H, J-K**: ns indicates not significantly different,
1030 *p<0.05, **p < 0.01, ***p<0.001, ****p < 0.0001, two-way ANOVA with Šidák's multiple
1031 comparisons test.

1032

1033

1034

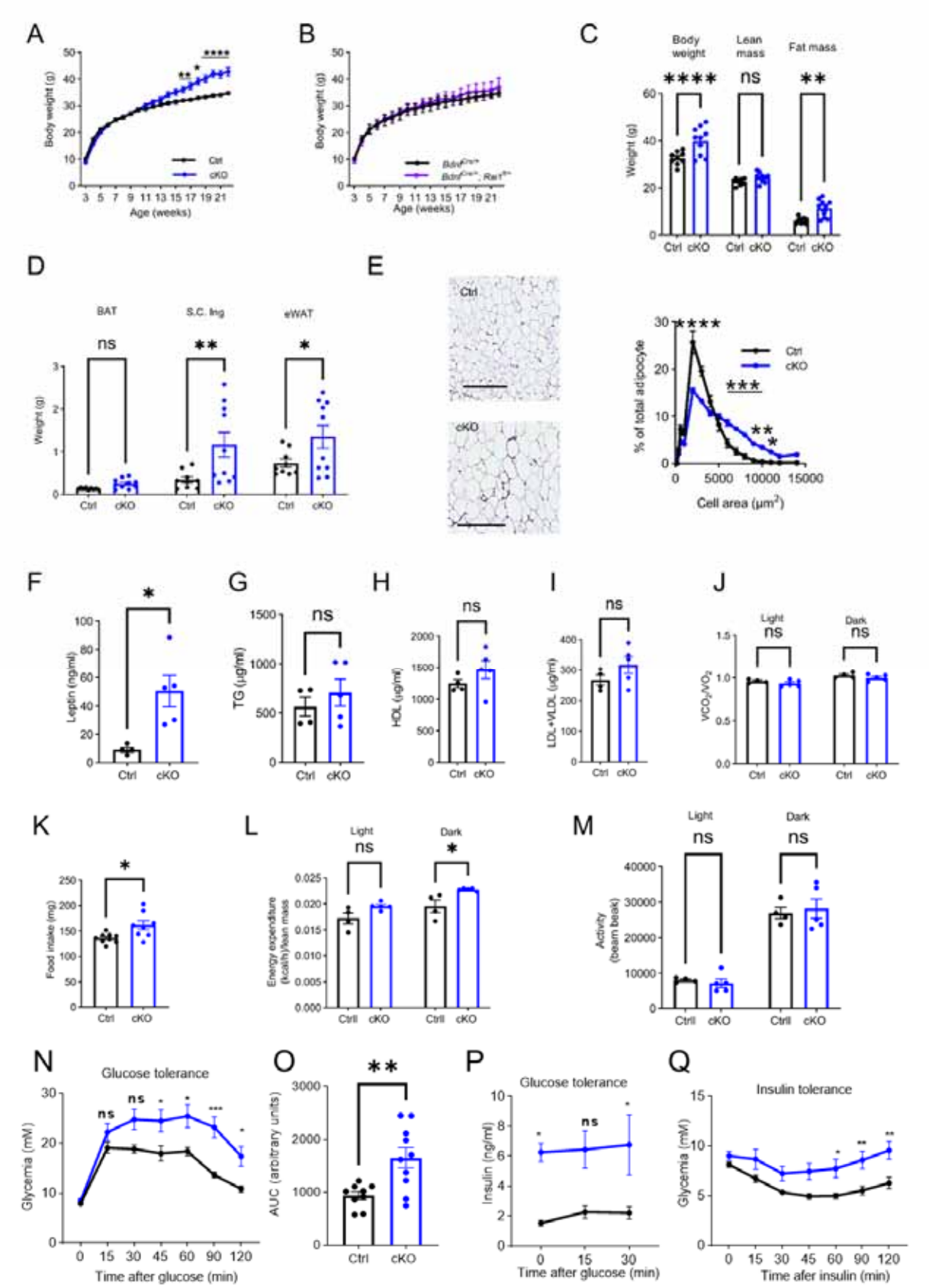

Fig 2-figure supplement 4

1035

1036 **Fig 2-figure supplement 4: Metabolic profiles of male cKO mice lacking Rai1 expression in**
1037 **the Bdnf-producing cells**

1038 **(A)** Male cKO mice gained significantly more weight than Ctrl mice beginning at 15 weeks of
1039 age.

1040 **(B)** Male *Bdnf*$^{Cre/+}$ and *Bdnf*$^{Cre/+}$; *Rai1*$^{fl/+}$ mice had similar body weights.

1041 **(C)** Echo-MRI analysis showed that 26-week-old male cKO mice had a significantly increased
1042 body weight due to increased fat but not lean mass. **p<0.01, ****p<0.0001, student's t-test.

1043 **(D)** Fat disposition analysis showing the weight of brown adipocytes (BAT), subcutaneous
1044 inguinal (S.C.ing), and epididymal white adipose tissues (eWAT). ns indicates not significantly
1045 different, *p<0.05, **p<0.01, student's t-test.

1046 **(E)** Male cKO mice showed eWAT cell hypertrophy. Top: Representative images of the eWAT
1047 tissues in Ctrl and cKO mice. Scale bar = 500µm. Bottom: Frequency distribution of cellular
1048 sizes.

1049 **(F-I)** Blood parameter analysis showing that male cKO mice showed significantly increased
1050 leptin levels **(F)** without alterations in TG **(G)**, HDL **(H)**, LDL+VLDL **(I)**. *p< 0.05, student's t-
1051 test.

1052 **(J)** No differences were found in respiratory exchange rate in male Ctrl and cKO mice.

1053 **(K)** Male cKO mice showed a significantly increased food intake compared to Ctrl littermates.
1054 *p< 0.05, student's t-test.

1055 **(L)** Male cKO mice showed increased energy expenditure at the dark phase.

1056 **(M)** Male Ctrl and cKO mice showed similar locomotor activities.

1057 **(N-P)** Glucose tolerance test shows that cKO male mice are glycemic 45 minutes post
1058 intraperitoneal glucose administration **(N)**, increased AUC **(O)**, despite significantly higher
1059 insulin levels before and 30 minutes after glucose administration **(P)**, suggesting potential insulin
1060 insensitivity.

1061 **(O)** Insulin tolerance test showing that male cKO mice showed significantly higher blood
1062 glucose levels 60 minutes after intraperitoneal insulin administration. **p<0.01, student's t-test.

1063 Data are shown as mean±SEM. Statistics for **A-B, E, J, L-N**, **P-Q**: ns indicates not significantly
1064 different, *$p<0.05$, **$p < 0.01$, ***$p<0.001$, ****$p < 0.0001$, one- or two-way ANOVA with
1065 Šidák's multiple comparisons test.

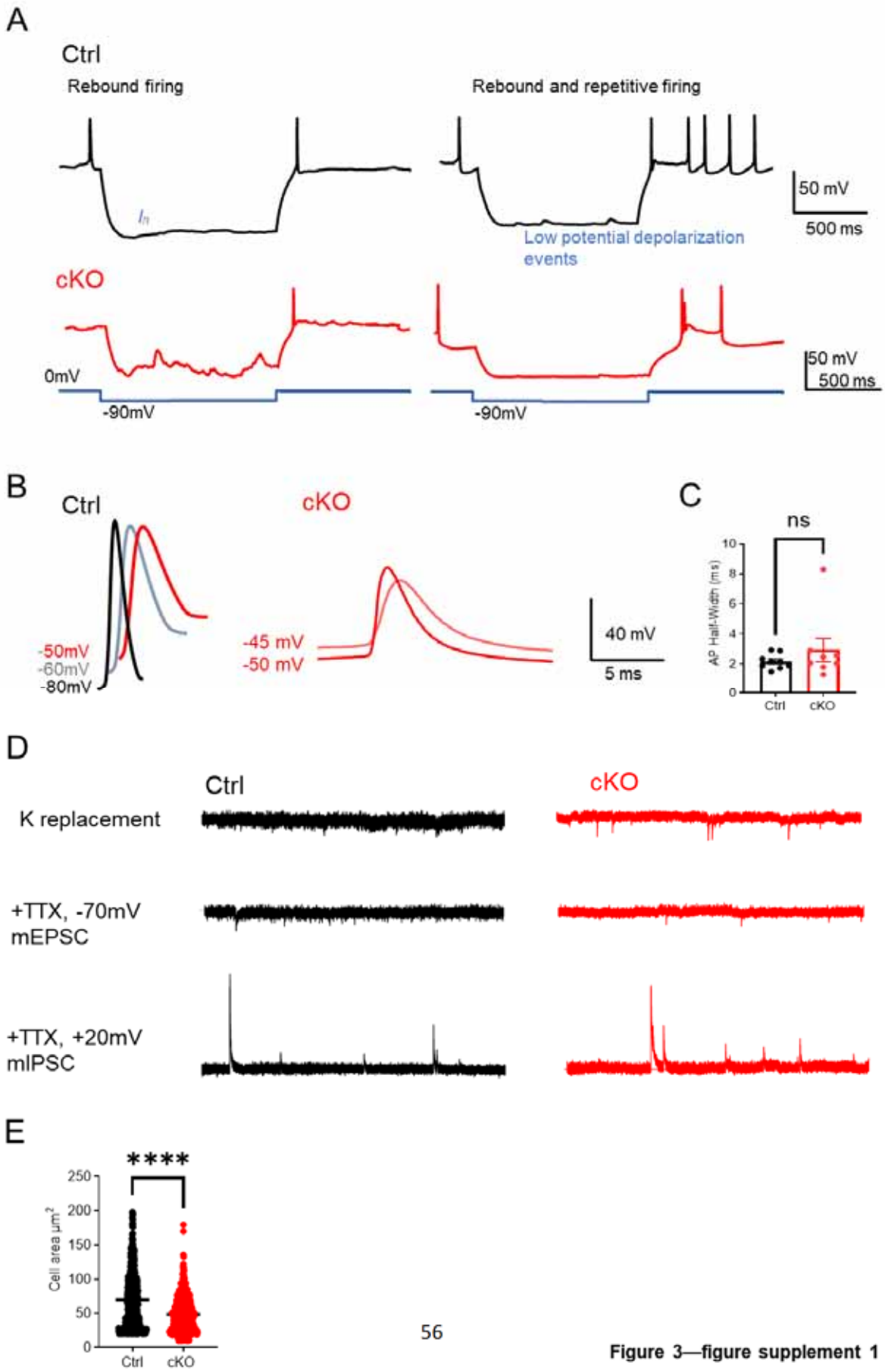

Figure 3—figure supplement 1

1066

1067 **Fig 3-figure supplement 1: The cellular and synaptic properties of control and Rai1-**
1068 **deficient PVH^{Bdnf} neurons**

1069 **(A)** Representative traces of rebound and rebound repetitive firing of PVH^{Bdnf} neurons in control
1070 (black) and cKO (red).

1071 **(B)** Representative AP waveforms at holding voltages of -70mV, -60mV, and -50mV in control
1072 (left) and -50mV and -45mV in cKO (right).

1073 **(C)** The half-width of AP initiated at a holding voltage of -60mV (neuronal numbers in brackets,
1074 p=0.374, student's t-test).

1075 **(D)** Representative traces of miniature recordings in control (black) and cKO (red) PVH^{Bdnf}
1076 neurons. The traces were recorded with a Cs-based internal at a holding voltage of -70mV in
1077 aCSF (top), spontaneous mEPSCs were recorded in aCSF containing 1uM TTX at a holding
1078 voltage of -70mV (middle), and mIPSCs were recorded at holding voltage of +10mV (bottom).

1079 **(E)** Quantification showing that the cellular size of cKO PVH^{Bdnf} neurons was significantly
1080 smaller than Ctrl neurons. ****$p<0.0001$, student's t-test.

1081

1082

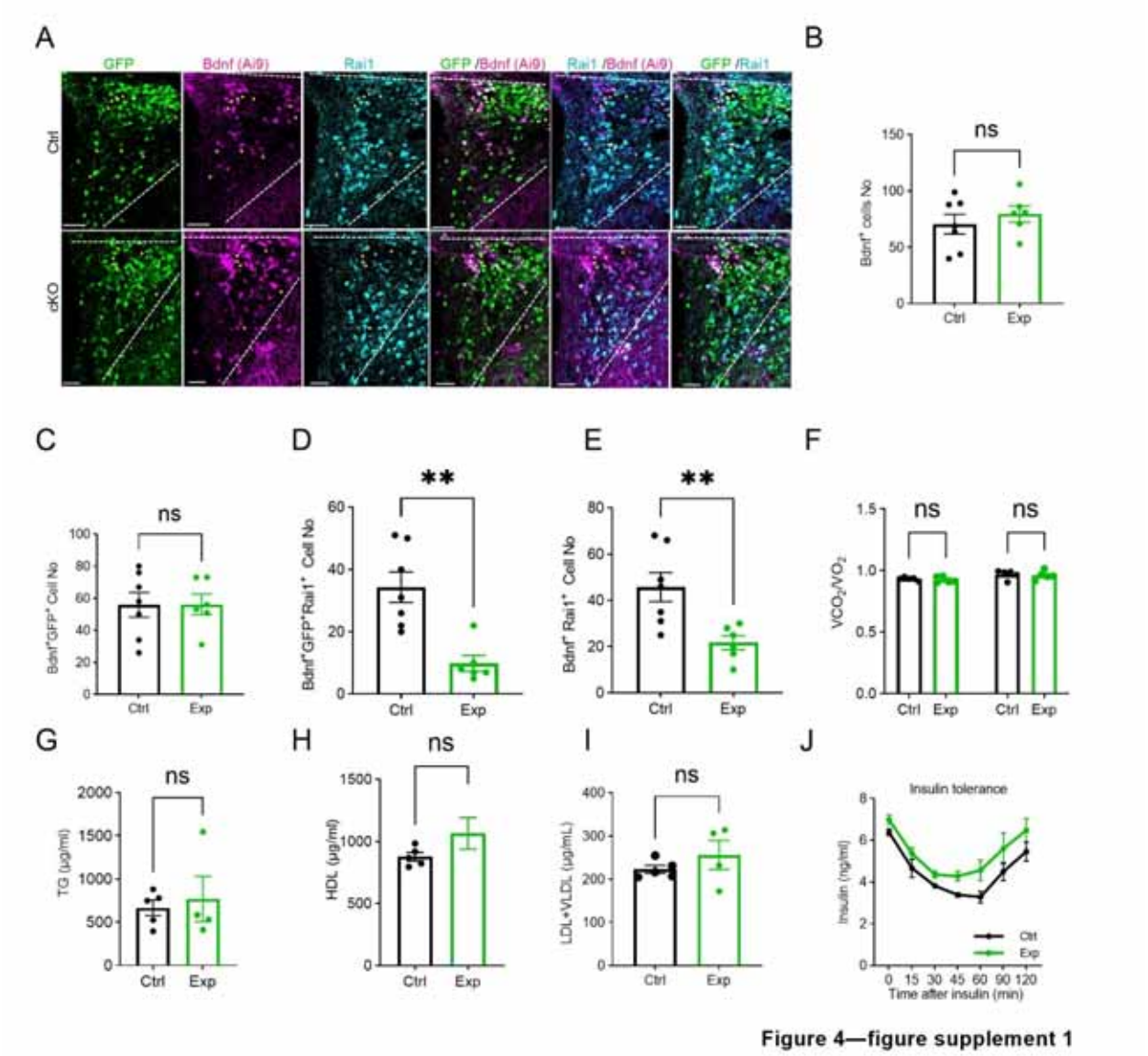

Figure 4—figure supplement 1

Fig 4-figure supplement 1: Metabolic profile of mice lacking *Rai1* in PVH^{Bdnf} neurons

(A) Representative images showing co-expression of virus-infected cells (GFP/green), *Bdnf*^{Cre}-dependent Ai9 signals (Bdnf cells, magenta), and endogenous Rai1 (cyan). Yellow arrowheads indicate Bdnf neurons infected with AAV and in these cells, Rai1 signals were diminished in Exp but not Ctrl mice. Scale bar = 50μm.

(B-C) The total number of PVH^{Bdnf} neurons **(B)** and total number of PVH^{Bdnf} neurons infected with AAVs **(C)** per slice showing that Rai1 deletion or virus infection did not alter the total number of PVH^{Bdnf} neurons.

1092 **(D)** Rai1 expression was significantly reduced in PVH^{Bdnf} neurons infected with both AAVs
1093 when compared to PVH^{Bdnf} neurons infected with sgRai1-GFP AAV alone.

1094 **(E)** The number of PVH^{Bdnf} neurons that co-express Rai1 was significantly reduced in the Exp
1095 group. **(F)** Respiratory exchange rate remained similar in Ctrl and Exp mice.

1096 **(G-I)** Blood parameter analysis showing the levels of TG, HDL, and LDL+VLDL were similar
1097 in Ctrl and Exp mice.

1098 **(J)** In the insulin tolerance test, Exp group showed a trend towards increased blood glucose level
1099 after insulin injection.

1100 Data are shown as mean±SEM. Statistics for **F**, **J**: ns indicates not significantly different, two-
1101 way ANOVA. Statistics for **B-E**, **G-I**: **$p<0.01$, student's t-test.

1102

1103

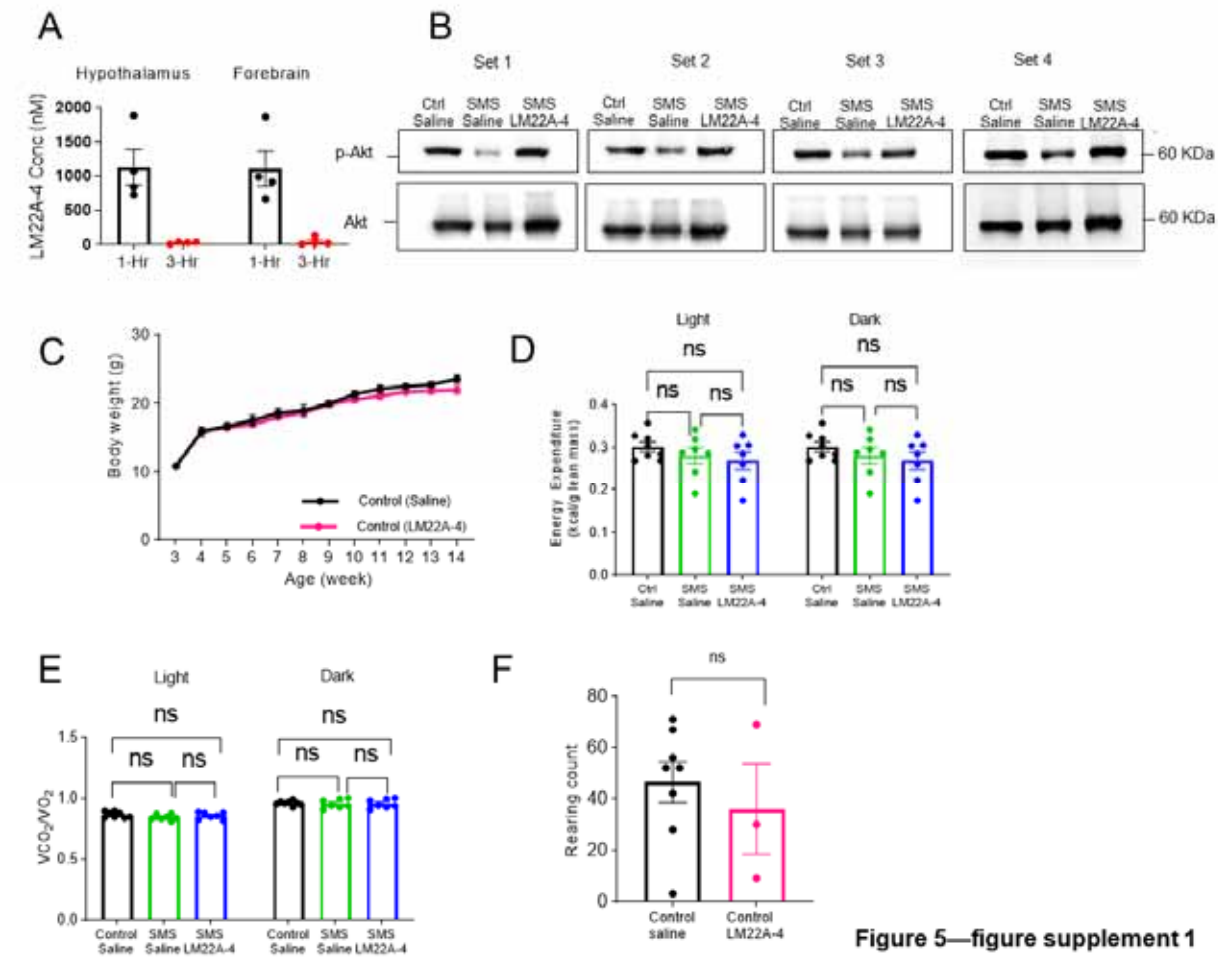

1104

1105 **Figure 5—figure supplement 1: LM22A-4 treatment does not disrupt energy homeostasis**
1106 **and repetitive rearing in the Ctrl mice**

1107 **(A)** LM22A-4 concentration in the hypothalamus and forebrain of SMS mice 1 hour (black dots)
1108 and 3 hours (red dots) after simultaneous intranasal and IP injections.

1109 **(B)** Four independent sets of western blotting analyses showing reduced p-Akt levels in the
1110 hypothalamus of saline-treated SMS mice, which were increased by LM22A-4 treatment. Total
1111 Akt protein was used as a control.

1112 **(C)** Similar body weight of Ctrl mice treated with either saline or LM22A-4.

1113 **(D)** Energy expenditure was not different between groups in the light vs. dark phase.

1114 **(E)** Respiratory exchange rates were not different between groups in the light vs. dark phase.

1115 **(F)** Repetitive rearing behaviour in Ctrl mice was not altered by LM22A-4 treatment. ns
1116 indicates not significantly different, student's t-test.

1117 Data are shown as mean±SEM. Statistics for **C-E**: ns indicates not significantly different, two-
1118 way ANOVA. Statistics for **F**: student's t-test.

1119

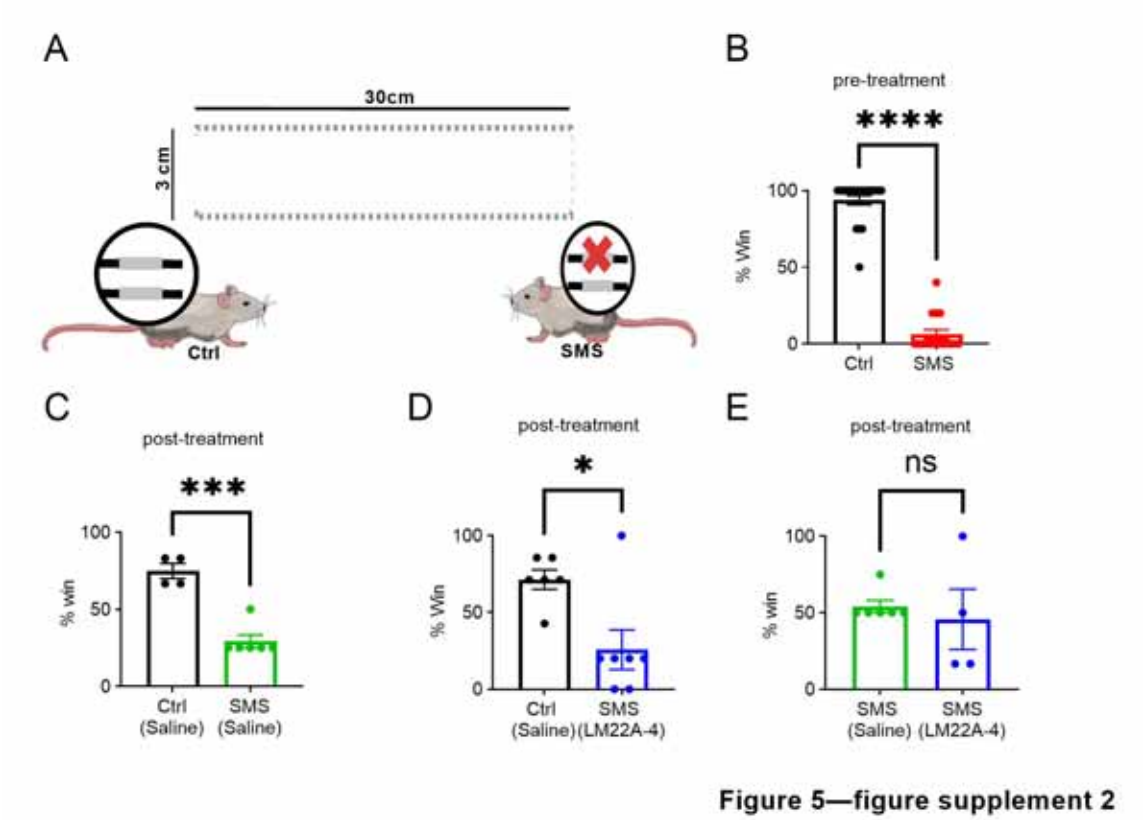

Figure 5—figure supplement 2: LM22A-4 treatment in adult SMS mice is insufficient to improve social interaction deficit

(A) Schematic showing the tube test that assesses social interaction between stranger mice of different genotypes.

(B) 7-week-old Ctrl mice won significantly more than SMS mice before the LM22A-4 treatment.

(C) 10-week-old saline-injected Ctrl mice won significantly more than the saline-injected SMS mice (two weeks post-LM22A-4 treatment).

(D) 10-week-old saline-injected Ctrl mice won significantly more than LM22A-4 injected SMS mice.

(E) 10-week-old saline-injected Ctrl mice showed a similar winning rate to LM22A-4-injected SMS mice.

Data are shown as mean±SEM. Statistics for **B-E**, ns indicates not significantly different, *p<0.05, ***p<0.001, ****p<0.0001, student's t-test.